Electronic Supplementary Information (ESI)

Boosting photoelectrochemical performance of $ZnIn_2S_4$ photoanodes via antimony-induced defect and surface homojunction engineering

Yequan Xiao,‡[a] Niu Wang,‡[a] Ziyi Zhang,[a] Yujie Zou,[a] Bowen Li,[b] Zeyu Fan,[d] Ronghua Li,[d] Yulong Qiao,[b] Ting Xiao,[a] Lihua Jiang,[a] Haijiao Xie,[f] Jingfu He,[c] Xiaobo Chen,[a] Yanbo Li,[d] Changli Li,*[c] Xinyu Tan*[a, e]

[a] *Hubei Provincial Engineering Research Center for Solar Energy High-value Utilization and Green Conversion, College of Materials Science and Engineering, China Three Gorges University Yichang, Hubei 443002, P. R. China.*

[b] *College of Electrical Engineering & New Energy, China Three Gorges University Yichang, Hubei 443002, P. R. China.*

[c] *School of Materials, Sun Yat-sen University, Shenzhen 518107, P. R. China*

[d] *Institute of Fundamental and Frontier Sciences, University of Electronic Science and Technology of China, Chengdu, 610054, P. R. China.*

[e] *School of New Energy, Jingchu University of Technology, Jingmen, Hubei, 448000, PR China*

[f] *Hangzhou Yanqu Information Technology Co., Ltd., Hangzhou, Zhejiang 310003, P. R. China.*

‡ These authors contributed equally to this work.

* Email: lichli5@mail.sysu.edu.cn (C. Li); tanxin@ctgu.edu.cn (X. Tan).

Contents

Experimental Section

1.1. Preparation of materials

$ZnIn_2S_4$ nanosheets were synthesized on FTO conductive glasses substrates via a facile hydrothermal method. Briefly, FTO glass (50×10 mm^2, ≤14 Ω sq^{-1}) was sequentially ultrasonically cleaned in acetone, isopropanol, and deionized (DI) water for 15 min each. The cleaned substrates were then placed into a 100 mL Teflon-lined stainless-steel autoclave, tilted against the wall with the conductive side facing downward. The Teflon liner contained a precursor solution prepared by dissolving 0.0068 g of zinc chloride ($ZnCl_2$, Aladdin, 99.95%), 0.22 g of indium chloride tetrahydrate ($InCl_3 \cdot 4H_2O$, Aladdin, 99.9%), and 0.30 g of thiourea (CH_4N_2S, Aladdin, 99%) in 50 mL of DI water under constant stirring for 10 min at room temperature. The sealed autoclave was heated at 170 °C for 12 h and naturally cooled to room temperature. The obtained $ZnIn_2S_4$ films on FTO substrate were rinsed with DI water and air-dried at room temperature, denoted as as-prepared $ZnIn_2S_4$.

To obtain oxygen-substituted $ZnIn_2S_4$ (O-$ZnIn_2S_4$), the as-prepared samples were annealed in air at 400 °C for 1 h with a heating rate of 5 °C min^{-1}. For Sb modification, antimony trichloride ($SbCl_3$, Aladdin, 99%) was dissolved in 1-methoxy-2-propanol to prepare solutions with concentrations of 1, 3, 5, 8, 10, and 20 mM. Then, 30 μL of each solution was spin-coated onto an 8 × 8 mm^2 area of the $ZnIn_2S_4$ samples using a two-step spin-coating program of 800 rpm for 10 s, followed by 3000 rpm for 60 s. The spin-coated $ZnIn_2S_4$ photoanodes were subsequently annealed in air at 400 °C for 1 h, following the same procedure as O-$ZnIn_2S_4$ to obtain Sb:O-$ZnIn_2S_4$ samples.

1.2. Materials characterization

The morphology and composition of samples were characterized using a Zeiss NVision 40 field-emission SEM associated with an EDS (Oxford Ultim Max 40). The crystal structures were analyzed by XRD diffraction on Thermo Scientific ARL EQUINOX 1000 diffractometer using Cu Kα radiation (40 kV and 30mA). Raman spectra were collected with a HORIBA JY LabRAM HR Evolution spectrometer using a 520 nm excitation wavelength. HAXPES was performed on PHI Quantes with a monochromatic Cr Kα X-ray source (5414 eV) and a 100 µm beam size. Room-temperature PL spectra were measured using a Picoquant FluoTime300 spectrometer, while TRPL spectra were acquired on the same instrument using 420 nm picosecond laser pulsed at a repetition rate of 40 MHz as the excitation sources. UV-vis absorbance spectra were recorded with a Shimadzu UV-3600 Plus spectrophotometer. UPS measurements were conducted using a He I (21.22 eV) excitation line, and the work function was determined from the UPS spectra by subtracting their width (that is, the energy difference between the analyses Fermi level and the high binding energy cut-off), from the He I excitation energy. XPS depth profiles were performed by etching the samples with 4 keV argon cluster ions (average cluster size of 500). Quantitative XPS analyses were carried out using Thermo Fisher Scientific Avantage Software[6.9k].

1.3. DFT calculations

DFT calculations were performed using the Vienna Ab initio Simulation Package (VASP) with the projector augmented wave (PAW) method.[1-3] The Perdew-Burke-Ernzerhof (PBE) functional within the generalized gradient approximation (GGA) was

used to describe the exchange-correlation potential.[4] A vacuum layer of 15 Å was applied to avoid interactions between periodic images. The plane-wave cutoff energy was set to 450 eV, and a 2 × 2 × 1 *k*-point mesh was used. Guided by XRD and SEM analyses showing a hexagonal nanosheet structure, a 3 × 3 × 1 supercell monolayer $ZnIn_2S_4$ exposing the (002) surface (with 63 total atoms, 9 Zn atoms, 18 In atoms and 36 S atoms) was constructed. Considering the presence of In vacancies in the as-prepared $ZnIn_2S_4$ indicated by quantitative analyses, models containing two In vacancies (established by removing the two In atom) were adopted as the initial configuration for the O-for-S substitution. Sb- and O- substituted models were generated by introducing Sb atoms into In vacancies and substituting O-for-S atoms. All structures were relaxed until the convergence tolerances of energy and force were less than 1.0×10^{-5} eV and 2.0×10^{-2} eV/Å, respectively. The DFT-D3 method was used to describe the van der Waals interaction.[5] The formation energy (E_{form}) of O-for-S substituted systems was defined as:

$$E_{form} = E_{substituted} - E_{unsubstituted} - n\mu_O + n\mu_S \quad (1)$$

where $E_{substituted}$ and $E_{unsubstituted}$ are the total energies of O-substituted (with different n number of O atoms) and unsubstituted systems, respectively, and μ_O and μ_S are the chemical potential of O and S atoms, respectively.

1.4. PEC characterization

PEC measurements were carried out at room temperature on an electrochemical workstation (CHI 760e, CH Instruments Inc., China) using a conventional three-electrode cell with a Pt foil counter electrode and a saturated Ag/AgCl reference

electrode. Electrical contact to the prepared photoanodes was established by soldering a copper wire to the designated region of the FTO substrate using indium, followed by encapsulation with epoxy resin (Araldite) to serve as the working electrode. The exposed electrode area after encapsulation was determined using calibrated digital images and analyzed with ImageJ[1.53k] software (**Fig. S1**). A commercial AM 1.5G solar simulator (LCS-100, Newport Corporation, 94011A-ES) was employed as the light source, and the irradiance was adjusted to 100 $mWcm^{-2}$ using a certified reference cell (Konica-Minolta AK-200). Linear sweep voltammograms (*J-V* curves) were recorded in 0.5 Na_2SO_4 electrolyte (pH 6.8, measured using a combined pH electrode LE438 IP67 on an F2-Standard ion meter, Mettler Toledo) under an anodic scan at a rate of 10 $mV\ s^{-1}$. All the measured potentials versus Ag/AgCl reference electrode were converted to the potentials versus RHE according to the Nernst equation:

$$E_{RHE} = E_{Ag/AgCl} + 0.0591pH + 0.1976 \quad (2)$$

The ABPE was calculated from the *J-V* curves under AM1.5G illumination using the equation:[6]

$$ABPE = \left[\frac{J_{photo}(mA\ cm^{-2}) \times (1.23 - V_{app})(V)}{P_{AM1.5G}(mW\ cm^{-2})} \right] \times 100\% \quad (3)$$

where V_{app} is the applied potential versus RHE, J_{photo} is the photocurrent density measured under an applied bias, and $P_{AM1.5G}$ is the AM 1.5G simulated sunlight irradiance (100 $mW\ cm^{-2}$).

The IPCE spectra were measured at 1.0 V vs. RHE in 0.5M Na_2SO_4 electrolyte using a monochromatic light source generated form a 150W Xenon-arc lamp (Newport, model 66902) equipped with a monochromator (model 75160) and a Merlin lock-in

detector (model 70105). Measurements were conducted over the wavelength range from 300 to 600 nm with a 20 nm interval. The monochromatic light intensity at each wavelength was calibrated with a calibrated reference cell (Thorlabs PDS1010-CAL). The IPCE at a given wavelength (λ) was calculated using the following equation:[6]

$$\mathrm{IPCE}(\lambda) = \frac{1240(\mathrm{V}\times\mathrm{nm})}{\lambda(\mathrm{nm})} \times \frac{(J_{\mathrm{light}} - J_{\mathrm{light}})(\mathrm{mA\ cm^{-2}})}{P_{mono}(\mathrm{mW\ cm^{-2}})} \times 100\% \quad (4)$$

where 1240 V nm represents a multiplication of Planck constant (h) and the light speed (c), λ is the incident light wavelength (nm), P_{mono} is the monochromatic illumination power intensity, and J_{light} and J_{dark} are the current density under illumination and in the dark, respectively.

1.5. PEIS and Mott-Schottky measurements

The PEIS measurements were conducted in a frequency range of 0.2 Hz to 100 kHz with an amplitude of 15 mV under constant AM1.5M simulated sunlight illumination (100 mWcm^{-2}). The obtained PEIS data were analyzed using the Randles equivalent circuit model, and fitting was performed with ZView software (Scribner Associates). The effective capacitances associated with the CPEs were calculated using the expressions reported in the literature:

$$C_{\mathrm{bulk}} = Y_{0,1}^{1/n_1}\left(\frac{1}{R_{\mathrm{s}}} + \frac{1}{R_{\mathrm{trap}} + R_{\mathrm{ss}}}\right)^{n_1 - 1/n_1} \quad (5)$$

$$C_{\mathrm{ss}} = Y_{0,2}^{1/n_2}\left(\frac{1}{R_{\mathrm{trap}}} + \frac{1}{R_{\mathrm{ss}}}\right)^{n_2 - 1/n_2} \quad (6)$$

where C_{bulk} represents the bulk capacitance of the space-charge layer, C_{ss} denotes the

surface capacitance at the semiconductor/electrolyte interface, and Y and n are parameters from the CPE fitting related to the impedance behavior. The R_s accounts for the combined resistance from the electrolyte, external contact layers, and conductive substrate. The R_{trap} reflects the bulk charge transport resistance within the photoanode, while R_{ct} corresponds to the interfacial charge transfer resistance at the semiconductor/electrolyte interface.

Mott-Schottky measurements were performed under dark conditions, with an anodic potential scan at a 15 mV AC amplitude and frequencies of 0.1, 0.2, 0.3, and 0.4 kHz. The carrier density at each frequency was calculated, and the average value was used to determine the carrier density in 0.5 M Na_2SO_4 solution, following the Mott-Schottky equation:[7]

$$\frac{1}{C^2} = \frac{2}{\varepsilon_0 \varepsilon A^2 q N_D} \times (V - V_{fb} - \frac{k_B T}{q}) \quad (7)$$

where C is the space-charge capacitance, V is the applied potential versus RHE, V_{fb} is the flat-band potential versus RHE, N_D is the charge carrier density, ε_0 is the vacuum permittivity (8.854×10^{-14} C V^{-1} cm^{-1}), ε is dielectric constant of the semiconductor (taken as 4.7 for the $ZnIn_2S_4$,[7] k_B is Boltzmann constant (1.381×10^{-23} J K^{-1}), q is the electronic charge (1.602×10^{-19} C), and T is the absolute temperature.

1.6. Supplemented measurements and equations.

The OCP decays during the light on/off transient were recorded after illuminating the photoanodes for 10 min under the same conditions use in the PEC measurements. The carrier lifetime (τ_n) was calculated using the following equation [8]:

$$\tau_{\mathrm{n}} = \frac{k_{\mathrm{B}}T}{q}\left(\frac{d(\mathrm{OCP})}{dt}\right)^{-1} \tag{8}$$

where τ_{n} is the potential-dependent carrier lifetime, k_{B} is the Boltzmann constant, T is the temperature in Kelvin, q is the electronic charge, and $d(\mathrm{OCP})/dt$ represents derivative of the OCP transient decay.

The η_{sep} and η_{inj} were evaluated using the following equations:[9]

$$J_{\mathrm{abs}} = \frac{q}{hc}\int_{\lambda} \lambda E(\lambda)A(\lambda)d\lambda = \int_{\lambda} \frac{\lambda E(\lambda)A(\lambda)}{1240}d\lambda \tag{9}$$

$$\eta_{\mathrm{sep}} = J_{\mathrm{ph}}^{\mathrm{Na_2SO_3+Na_2S}} \Big/ J_{\mathrm{abs}} \tag{10}$$

$$\eta_{\mathrm{inj}} = J_{\mathrm{ph}}^{\mathrm{Na_2SO_4}} \Big/ J_{\mathrm{ph}}^{\mathrm{Na_2SO_3+Na_2S}} \tag{11}$$

Here, J_{abs} is the maximum photocurrent density, assuming that all the absorbed photons in the $ZnIn_2S_4$ samples are efficiently converted into electrical current. $E(\lambda)$ and $A(\lambda)$ both functions of photon wavelength (λ), where $E(\lambda)$ represents the spectral irradiance of the AM 1.5 G solar spectrum (ASTM G173-03), and $A(\lambda)$ denotes the absorbance of the $ZnIn_2S_4$ samples obtained from the UV-Visible absorption spectrum. The constants h, q, and c are the Planck constant, electronic charge, the light speed, respectively. In addition, $J_{\mathrm{ph}}^{\mathrm{Na_2SO_3+Na_2S}}$ is the photocurrent density measured in 0.35M Na_2SO_3 and 0.25M Na_2S mixed electrolyte, which served as hole scavengers, ensuring the hole injection rate approaching 100%. Meanwhile, $J_{\mathrm{ph}}^{\mathrm{Na_2SO_4}}$ is the photocurrent density measured in 0.5M Na_2SO_4, using the *J-V* curve data.

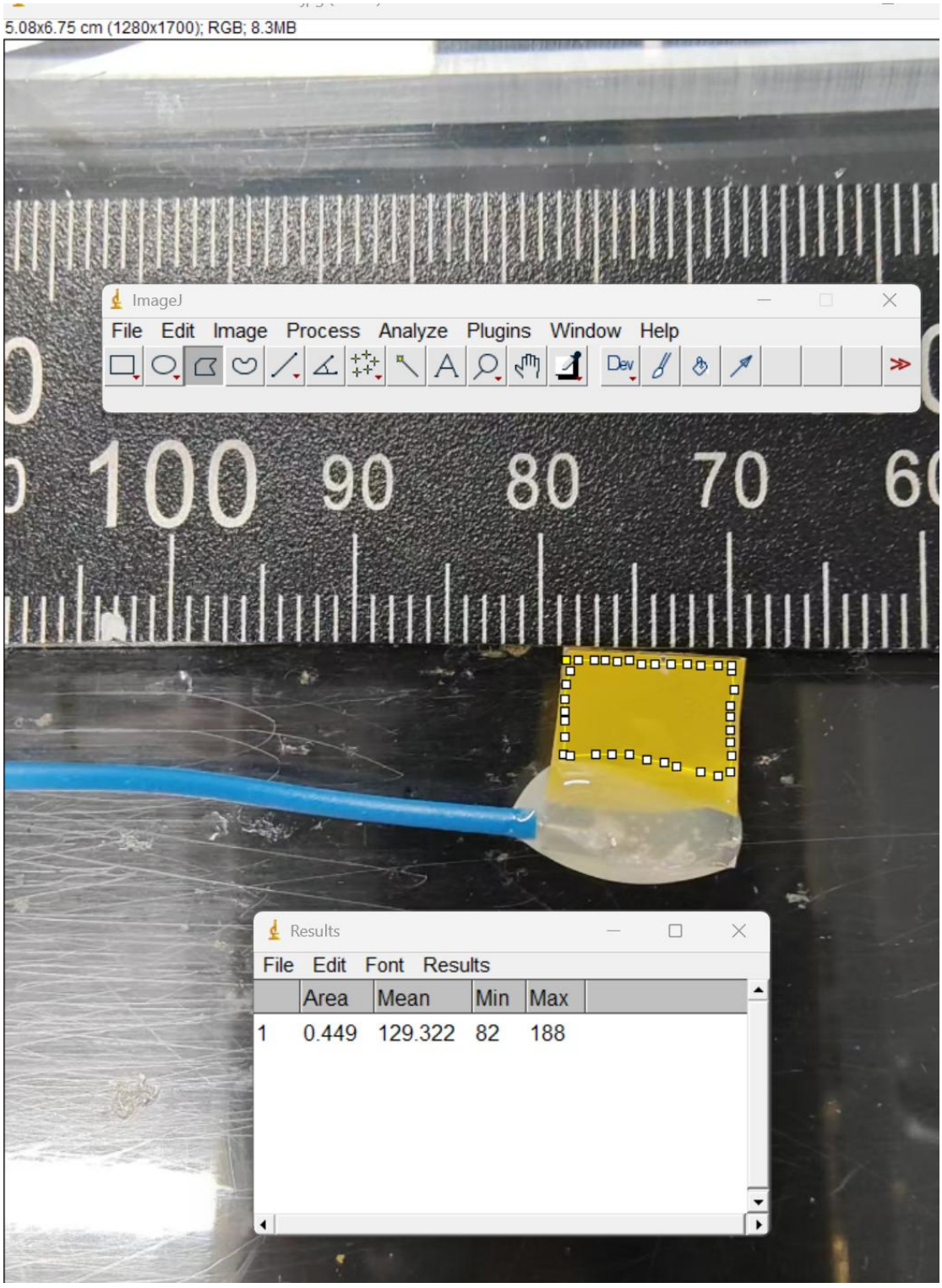

Fig. S1. Photographic image of fabricated photoanode. The exposed area of the electrode was measured with ImageJ1.53k software.

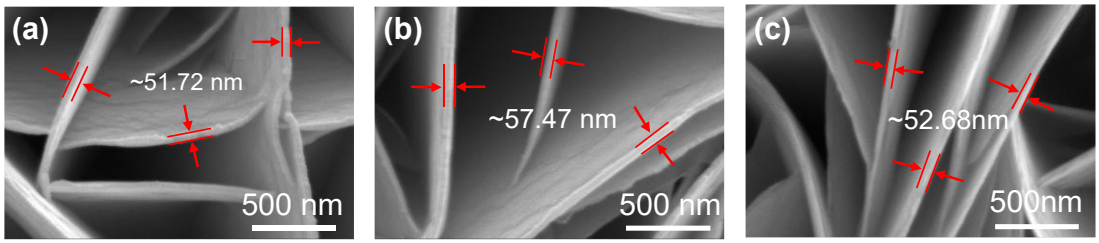

Fig. S2. Top-view SEM images for as-prepared $ZnIn_2S_4$ (a), O-$ZnIn_2S_4$ (b), and Sb:O-$ZnIn_2S_4$ (c) nanosheet films. All samples exhibit an ordered two-dimensional (2D) nanosheet morphology, with an average thickness of approximately 50 nm.

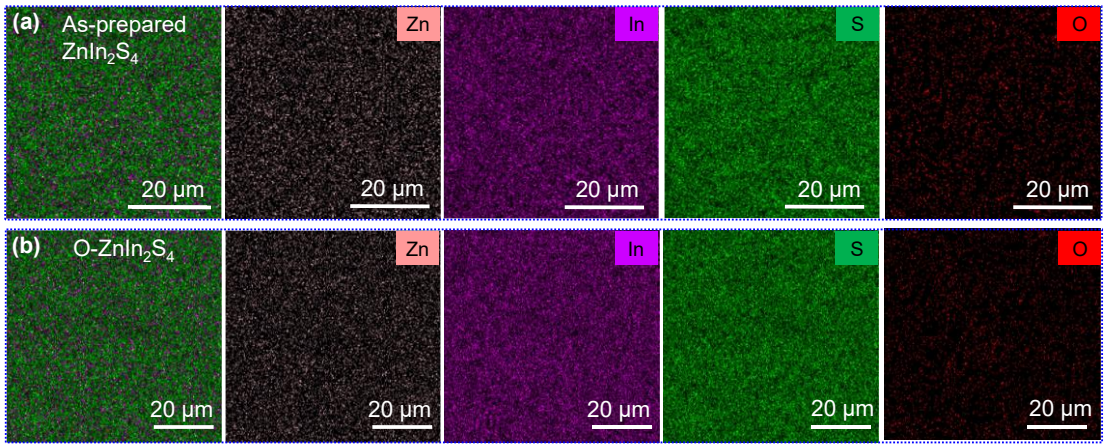

Fig. S3. SEM-EDS elemental mappings of as-prepared $ZnIn_2S_4$ (a) and O-$ZnIn_2S_4$ (b) samples.

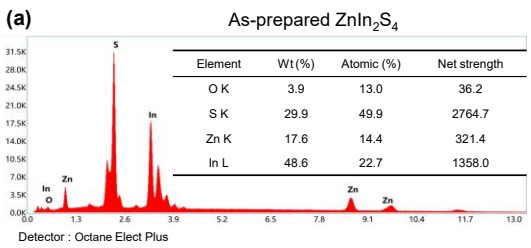

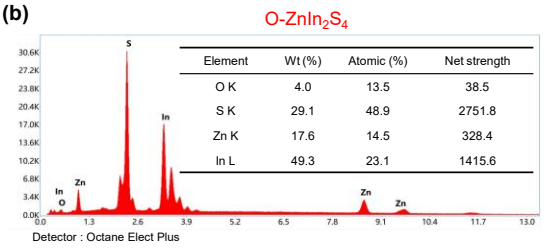

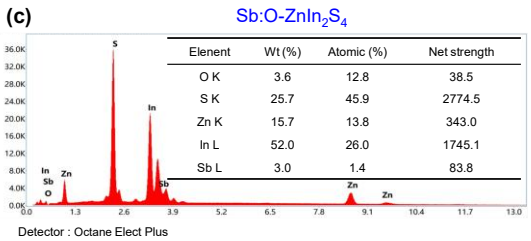

(d) Table. Atomic ratios of samples determined by EDS analysis

Sample	Atomic ratios				
	In/Zn	**S/Zn**	**O/S**	**O/(S+O)**	**Sb/(In + Sb)**
As-prepared $ZnIn_2S_4$	1.58	3.46	0.26	0.20	/
$O\text{-}ZnIn_2S_4$	1.59	3.37	0.27	0.21	/
$Sb\text{:}O\text{-}ZnIn_2S_4$	1.88	3.33	0.28	0.22	0.051

Fig. S4. (a-c) SEM-EDS elemental mappings analysis of as-prepared $ZnIn_2S_4$ (a), O-$ZnIn_2S_4$ (b), and Sb:O-$ZnIn_2S_4$ (c) samples. (d) The corresponding atomic ratios of the three samples were obtained through EDS mapping analysis.

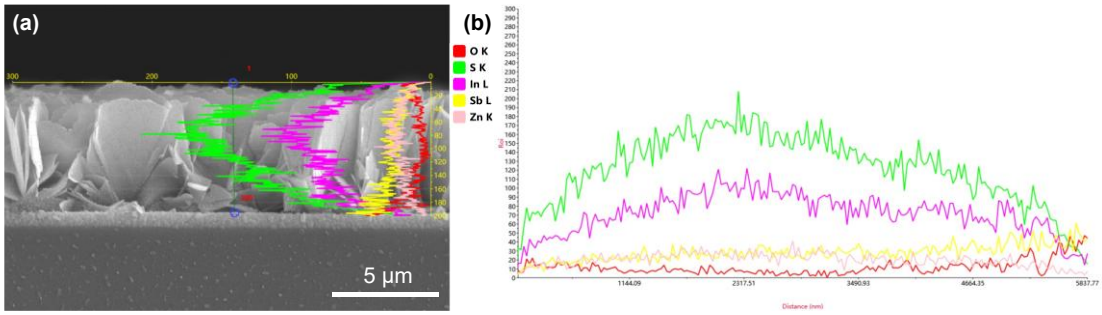

Fig. S5. STM-EDS line scan of elements (Zn, In, Sb, S, O) in the Sb:O-$ZnIn_2S_4$ sample.

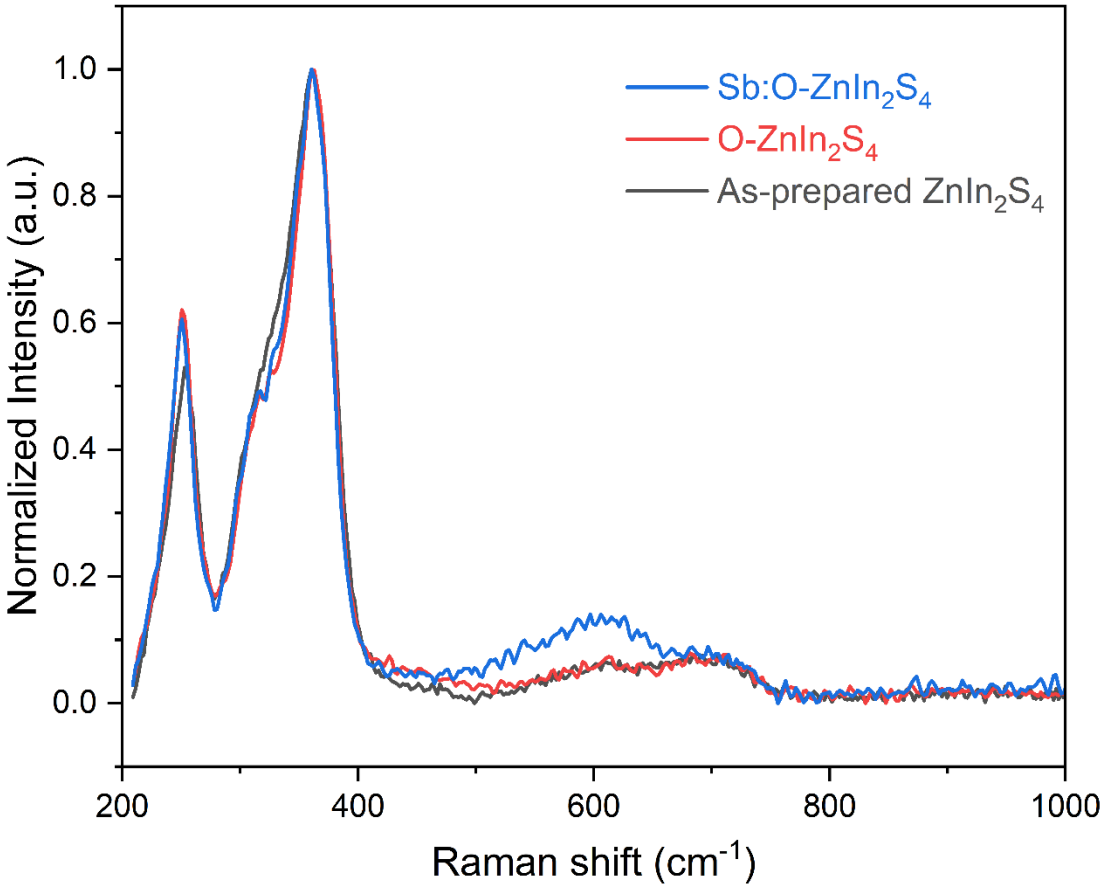

Fig. S6. Normalized Raman spectra of as-prepared $ZnIn_2S_4$, O-$ZnIn_2S_4$, and Sb:O-$ZnIn_2S_4$ samples.

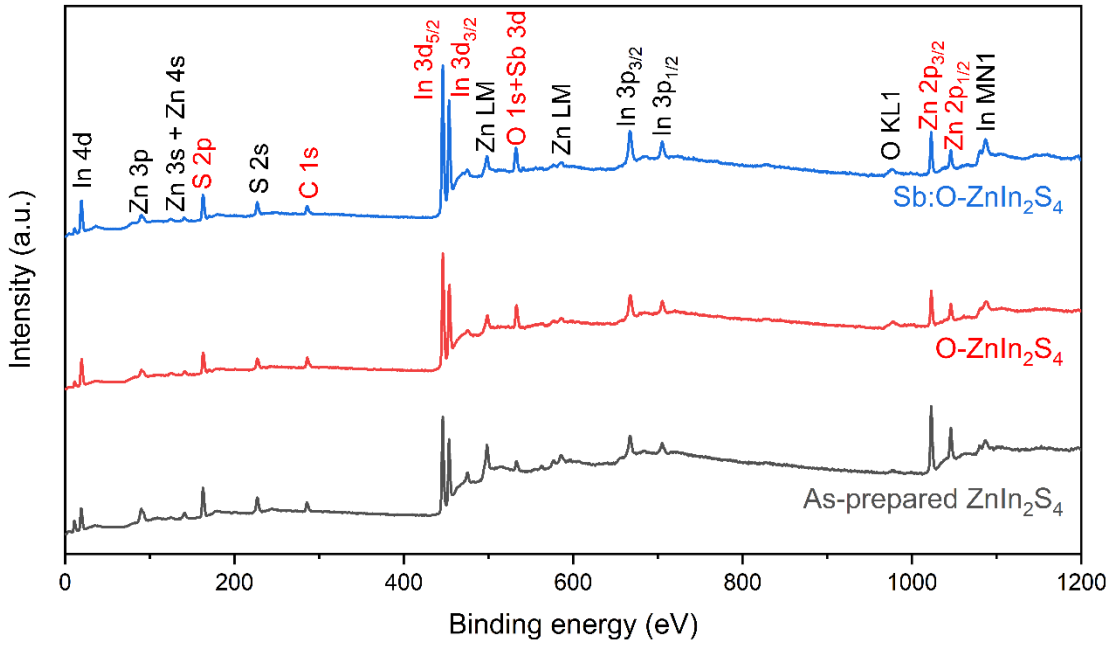

Fig. S7. XPS survey spectra of as-prepared $ZnIn_2S_4$, O-$ZnIn_2S_4$, and Sb:O-$ZnIn_2S_4$ samples. The charging shift for these spectra compensated using the C 1s at 284.8 eV as the reference.

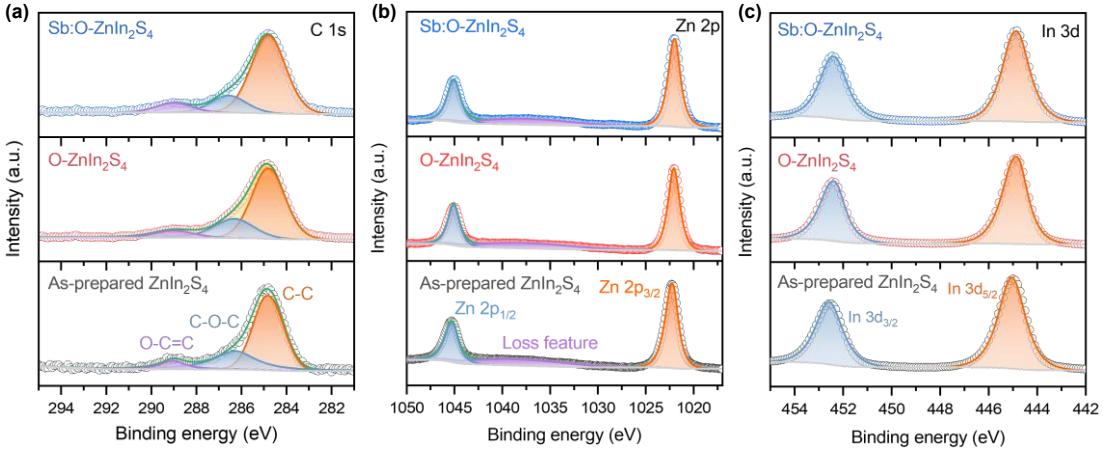

Fig. S8. XPS core-level spectra of C 1*s* (a), Zn 2*p* (b), and In 3*d* (c) for as-prepared $ZnIn_2S_4$, O-$ZnIn_2S_4$, and Sb:O-$ZnIn_2S_4$ samples.

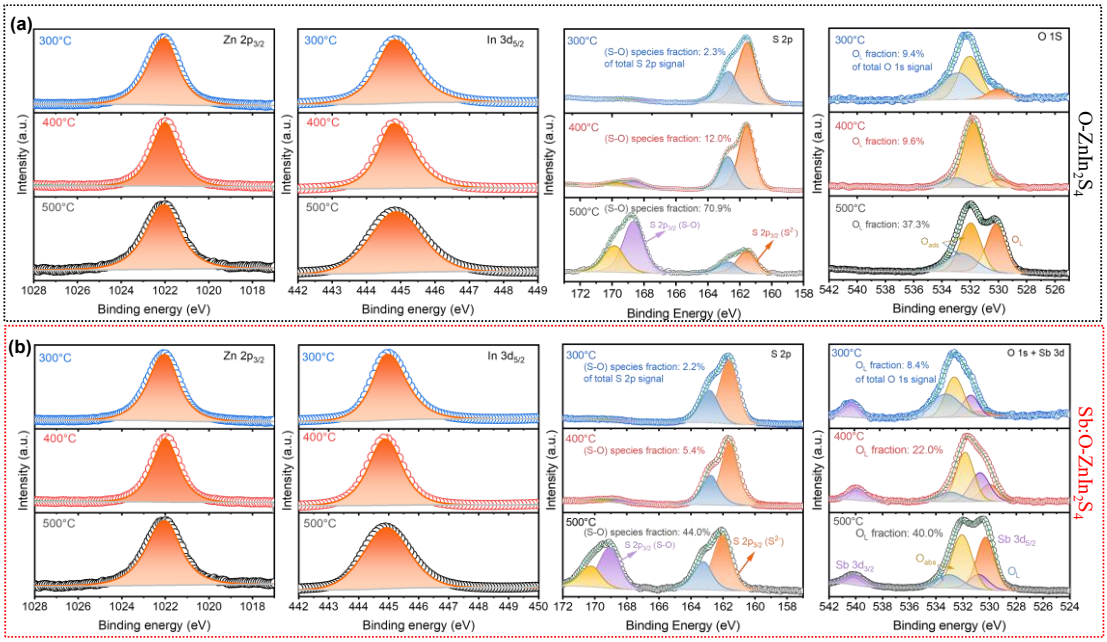

Fig. S9. Temperature-dependent HAXPES analysis of O-$ZnIn_2S_4$ (a) and Sb:O-$ZnIn_2S_4$ (b) after air annealing under identical conditions. S 2p spectra shows that S-O components increase with temperature in both cases but remains consistently lower in Sb:O-$ZnIn_2S_4$ than in O-$ZnIn_2S_4$ at the same temperature. Moreover, the lattice-related O fraction or O/(S+O) ratio versus annealing temperature shows a monotonic increase with temperature and consistently higher lattice O in Sb:O-$ZnIn_2S_4$ compared with O-$ZnIn_2S_4$ under identical annealing conditions. These results support that Sb promotes O incorporation into lattice/near-lattice configurations while mitigating sulfur over-oxidation during air annealing.

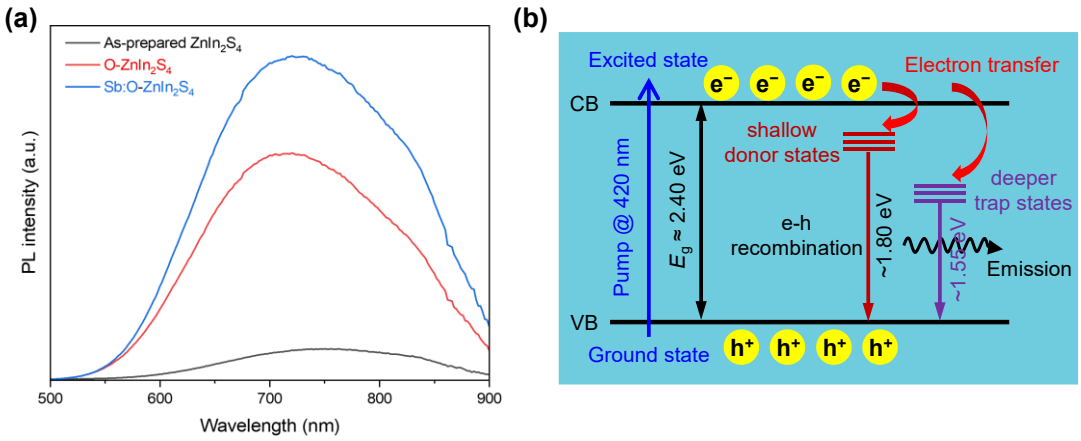

Fig. S10. (a) Room temperature PL spectra for as-prepared $ZnIn_2S_4$, O-$ZnIn_2S_4$, and Sb:O-$ZnIn_2S_4$ samples measured under 420 nm laser excitation. (b) Schematic illustration of the mechanisms involved in the PL emission related to defects in $ZnIn_2S_4$.

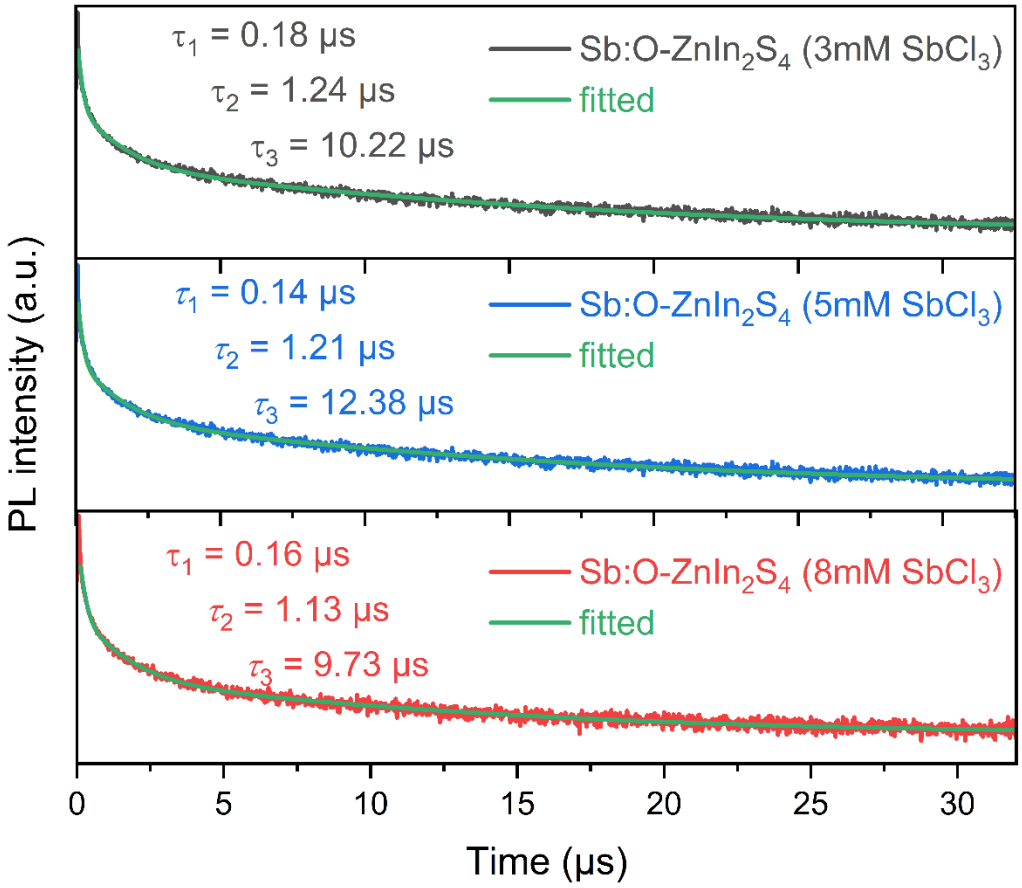

Fig. S11. TRPL decay curves of Sb:O-$ZnIn_2S_4$ samples with different $SbCl_3$ concentrations, recorded at about 690 nm under 420 nm laser excitation. TRPL provides direct kinetic evidence that moderate Sb incorporation suppresses trap-assisted recombination, whereas excessive Sb reverses this trend. The optimized 5 mM Sb sample shows the longest τ_{AV} (10.15 μs) and the largest f_3 (80.4%), accompanied by the smallest f_1 (4.1%) (**Table S1**), indicating suppressed non-radiative recombination via surface/interface traps. In contrast, at higher Sb concentration (8 mM), τ_{AV} decreases to 6.74 μs and f_3 drops to 66.3%, while both the f_1 (8.8%) and the f_2 (25.0%) increase, suggesting an increased population of non-radiative traps and deep/intermediate trap-mediated recombination pathways.

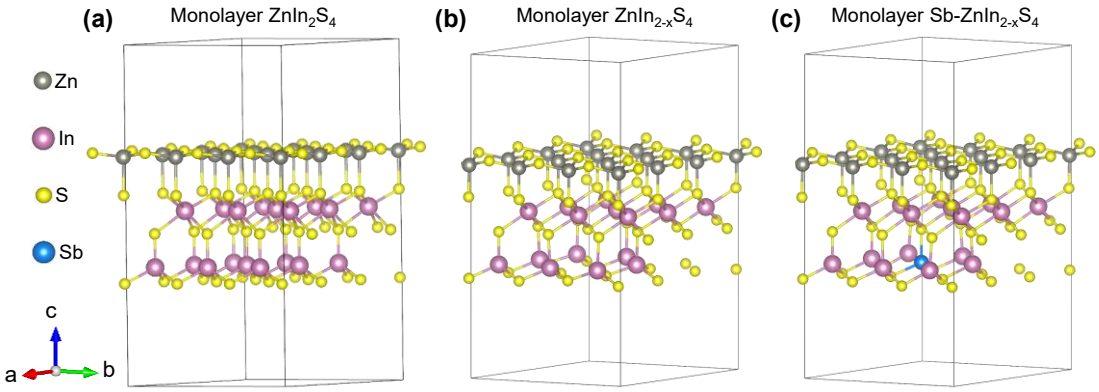

Fig. S12. (a) Constructed monolayer $ZnIn_2S_4$ supercell. (b) $ZnIn_2S_4$ supercell containing In vacancies (termed as $ZnIn_{2-x}S_4$), with an (In vacancy)/(total In atom) ratio of 0.1111. (c) $ZnIn_2S_4$ supercell (termed as Sb-$ZnIn_{2-x}S_4$) with partial substitution of In vacancies or In atoms by Sb, where the Sb/(Sb + In) ratio is 0.058 and the (In vacancy)/(total In atom) ratio is 0.056.

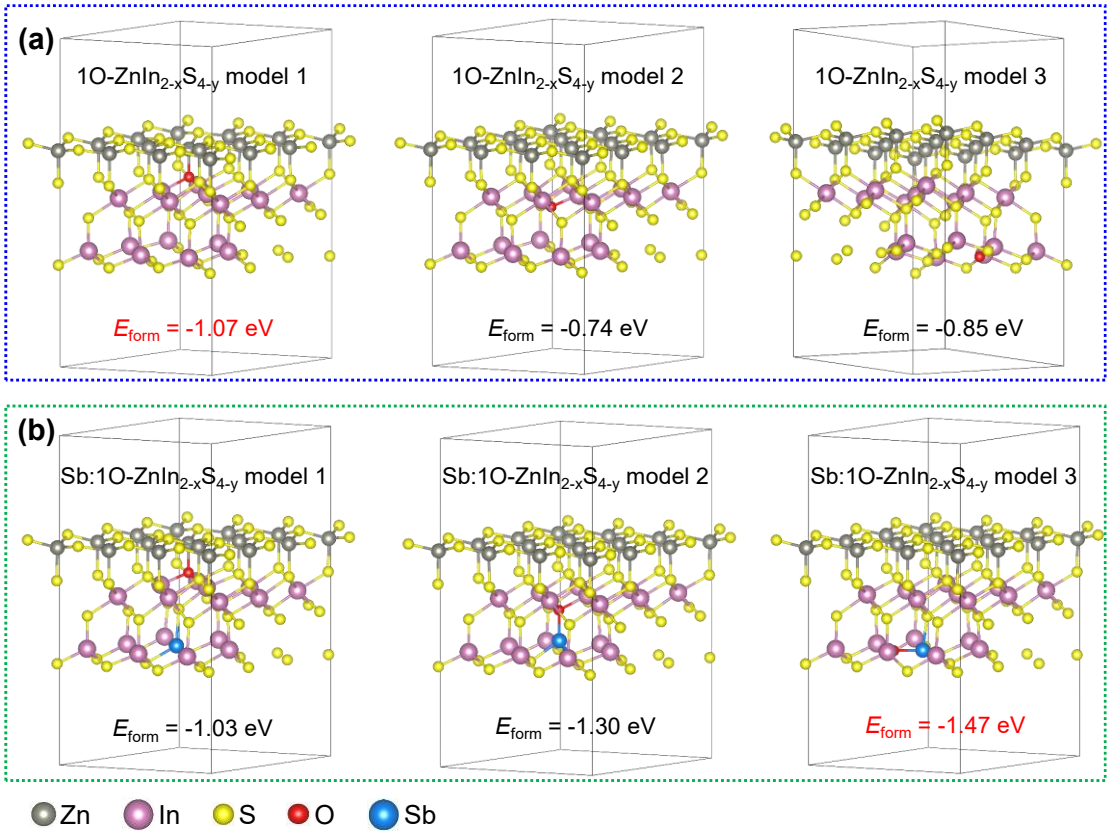

Fig. S13. (a) Simulated O-substituted $ZnIn_{2-x}S_4$ structures with one O atom replacing different equivalent S sites (denoted as 1O-$ZnIn_{2-x}S_{4-y}$) and their corresponding formation energies (E_{form}). The O/(O+S) ratio in this configuration is 0.0278. Model 1 exhibits the lowest E_{form}, indicating the most favorable single O-for-S substitution. (b) Simulated Sb- and O-cosubstituted $ZnIn_{2-x}S_4$ structures with one O atom replacing different equivalent S sites (termed as Sb:1O-$ZnIn_{2-x}S_{4-y}$) and their corresponding E_{form}. Upon Sb incorporation, Model 3 shows the lowest E_{form}, suggesting it represents the most stable structure at the same O substitution level.

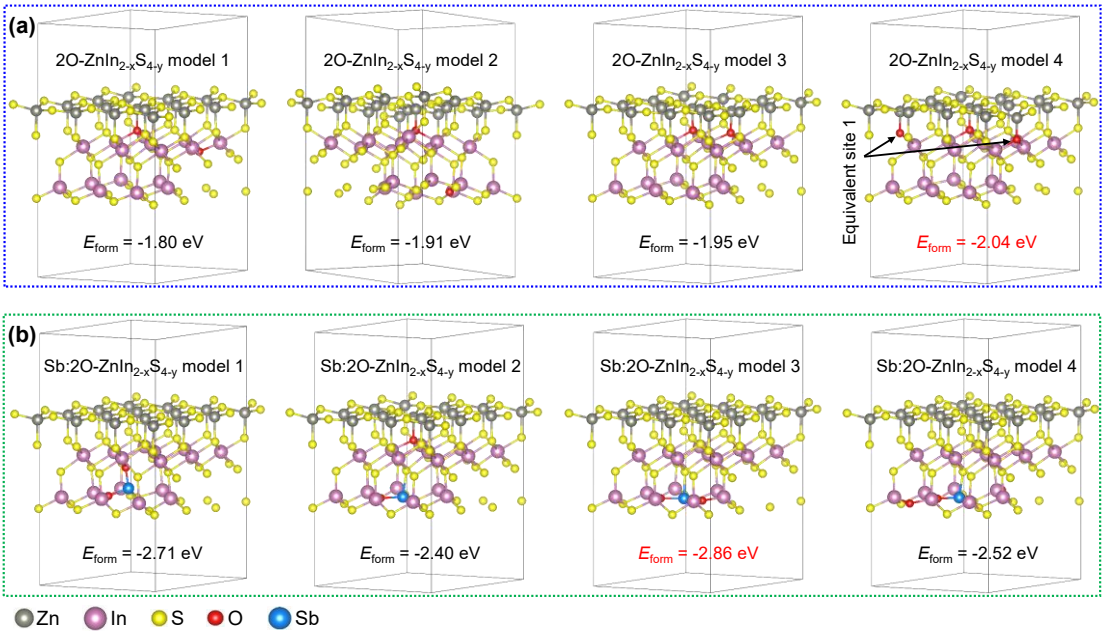

Fig. S14. (a) Simulated 2O-$ZnIn_{2-x}S_{4-y}$ structures and their corresponding E_{form}, where two O atoms substitute different equivalent S sites. The O/(O+S) ratio in this configuration is 0.0556. Model 4 represents the most favorable 2O-for-S substitution structure. (b) Simulated Sb:2O-$ZnIn_{2-x}S_{4-y}$ structures and their corresponding E_{form}. Model 3 is identified as the most stable structure.

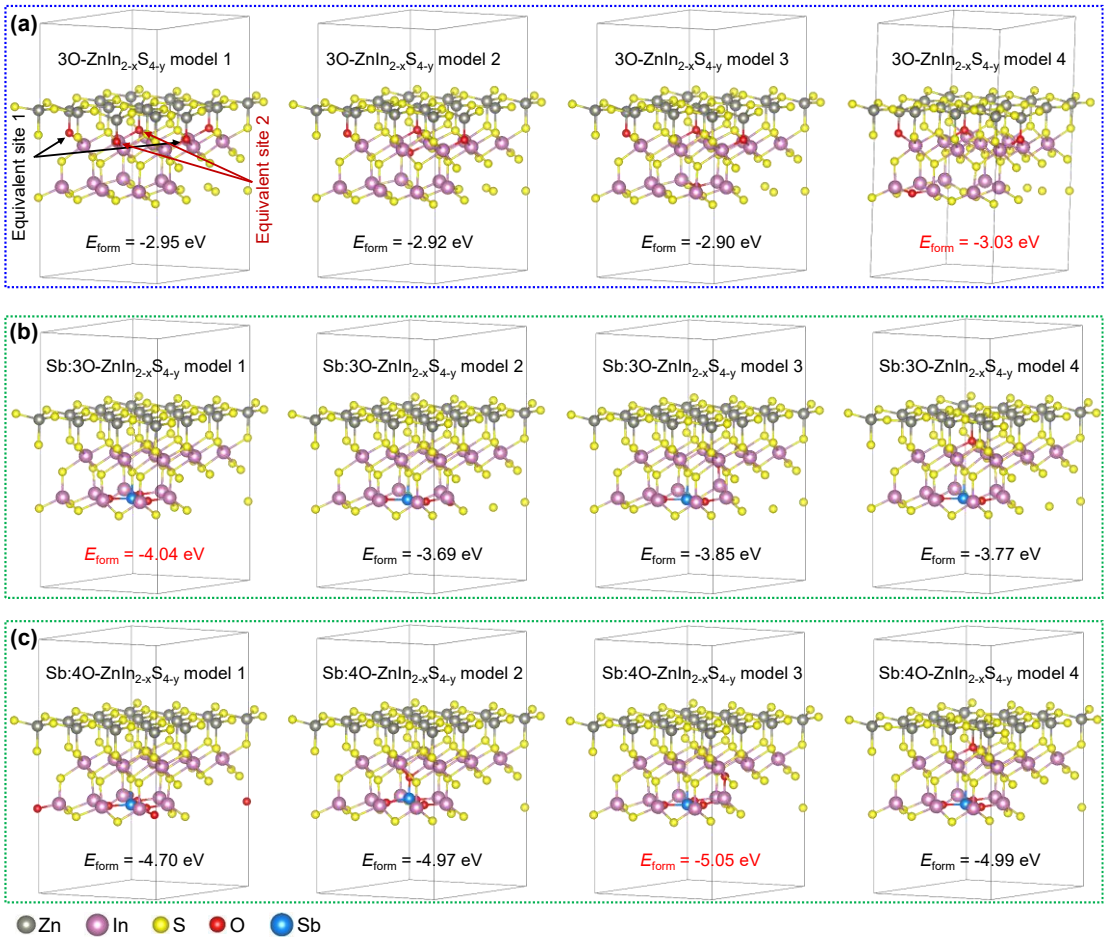

Fig. S15. (a) Simulated 3O-$ZnIn_{2-x}S_{4-y}$ structures with three O substituting different equivalent S sites and their corresponding E_{form}. The O/(O+S) ratio is 0.0833, close to the experimentally measured O content of the O-$ZnIn_2S_4$ sample. Model 5 exhibits the lowest E_{form} and was used as the structural model for subsequent density of state (DOS) and partial DOS (PDOS) calculations. (b) Simulated Sb:3O-$ZnIn_{2-x}S_{4-y}$ structures and their corresponding E_{form}, with Model 1 identified as the most stable structure. (c) Simulated Sb:4O-$ZnIn_{2-x}S_{4-y}$ structures with four O atoms substituting different equivalent S sites and their corresponding E_{form}. The O/(O+S) ratio is 0.1111, close to the experimental measured O content of the Sb:O-$ZnIn_2S_4$ sample, and model 3 was used for subsequent DOS and PDOS calculations.

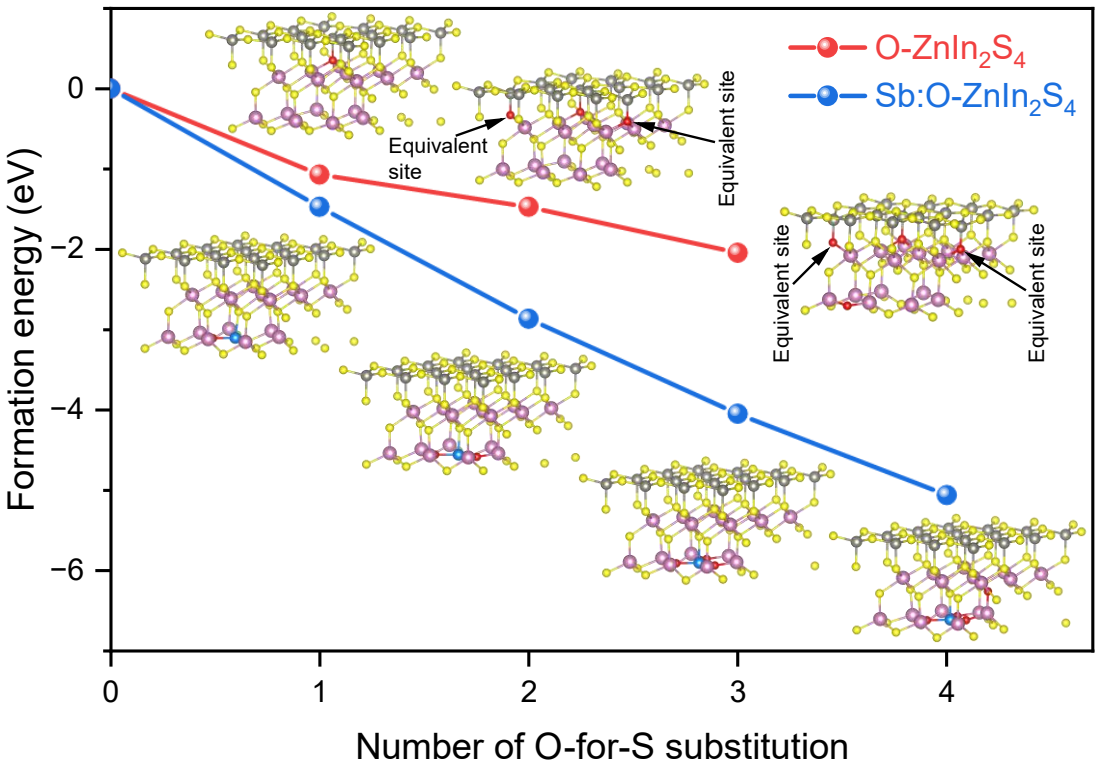

Fig. S16. Relationship between E_{form} and the number of O substitutions for the most stable structures in the O-$ZnIn_2S_4$ and Sb:O-$ZnIn_2S_4$ systems. Insets show the corresponding optimized structural models.

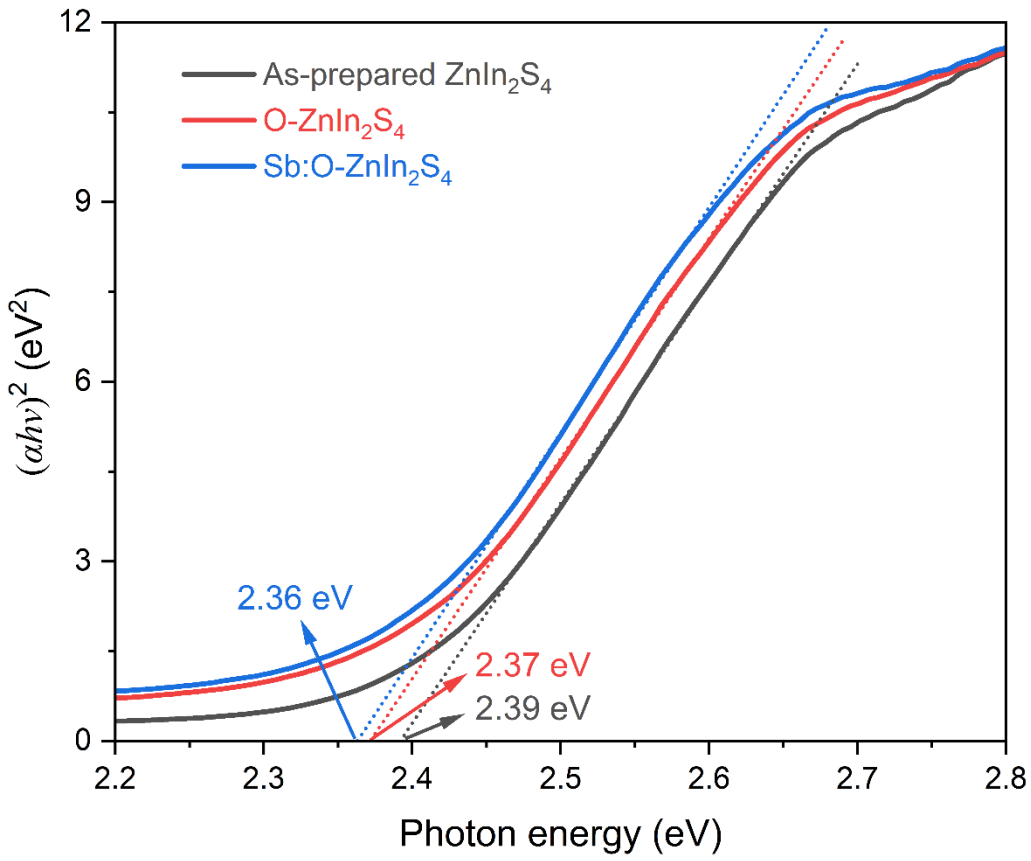

Fig. S17. Tauc plots of UV-vis absorption spectra for as-prepared $ZnIn_2S_4$, O-$ZnIn_2S_4$, and Sb:O-$ZnIn_2S_4$ samples. α, absorption coefficient; h, Planck constant; v, photon frequency.

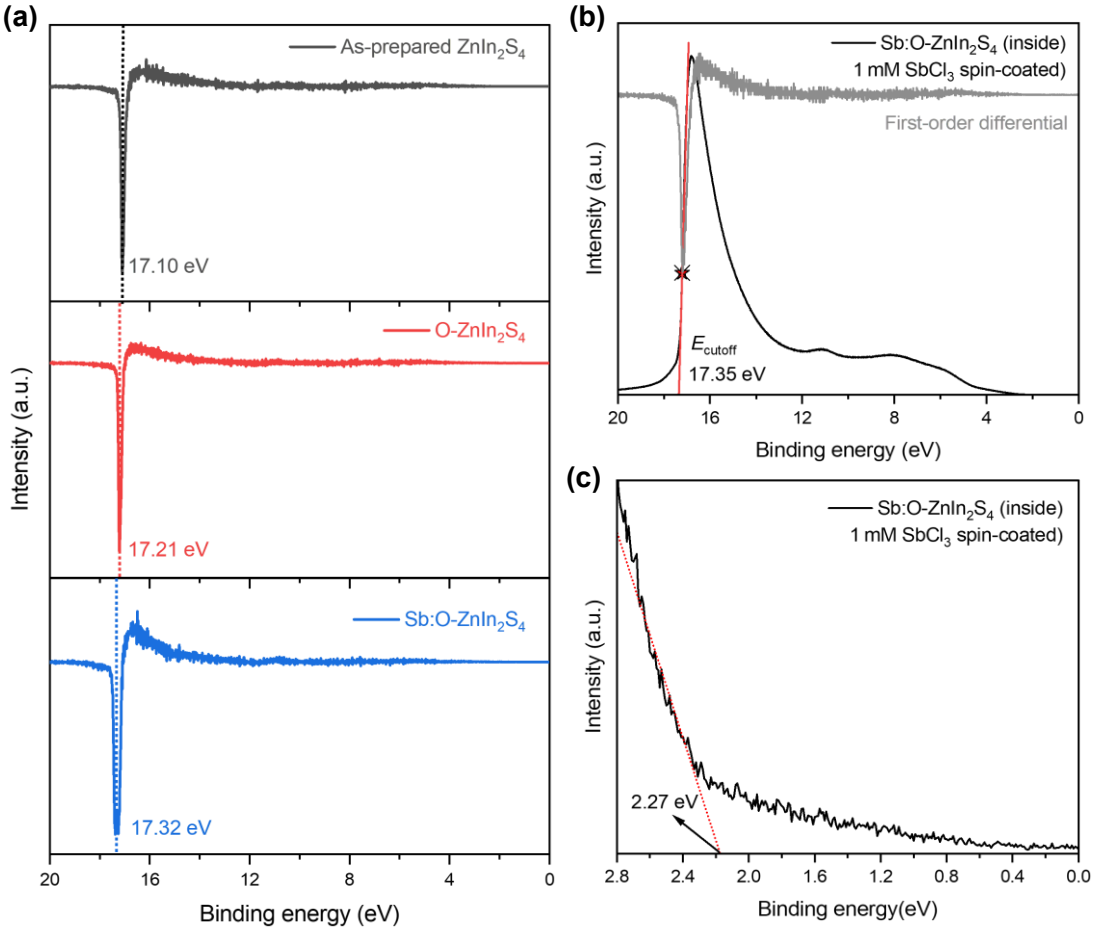

Fig. S18. (a) First-order differential of the UPS spectra for as-prepared $ZnIn_2S_4$, O-$ZnIn_2S_4$, and Sb:O-$ZnIn_2S_4$ samples. The minimum points of the first derivative curves correspond to the tangent points in the high binding energy region of the UPS spectra (**Fig. 4b**). The intersection of the tangent line with the X-axis defines the high binding energy cut-off (E_{cutoff}). (b) UPS spectra from the low Sb concentration region in Sb:O-$ZnIn_2S_4$ sample (denoted as Sb:O-$ZnIn_2S_4$ (inside)), obtained by spin-coating with a 1 mM $SbCl_3$ solution. (c) Valence band spectra of Sb:O-$ZnIn_2S_4$ (inside) in the low binding energy region of the UPS spectra, used to determine the valence band position.

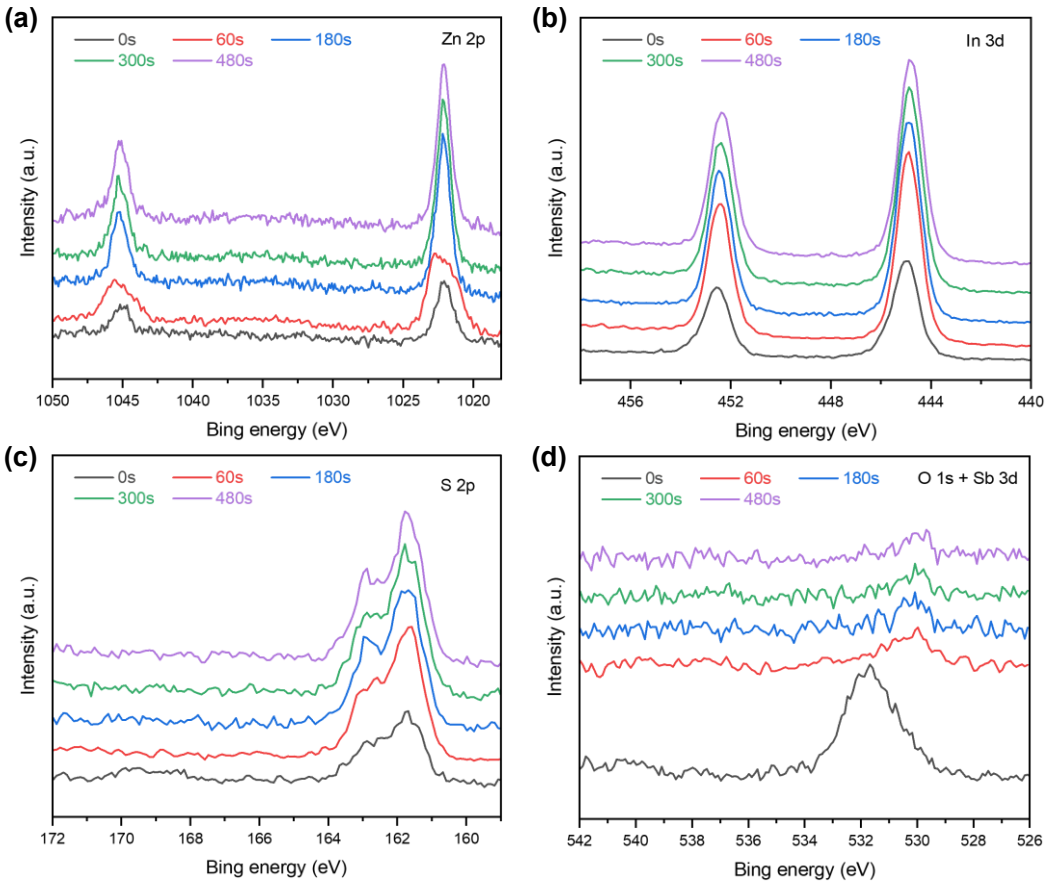

Fig. S19. XPS depth profile of the core-level spectra for Zn 2*p* (a), In 3*d* (b), S 2*p* (c), and (O 1*s* + Sb 3*d*) (d) in the Sb:O-$ZnIn_2S_4$ sample.

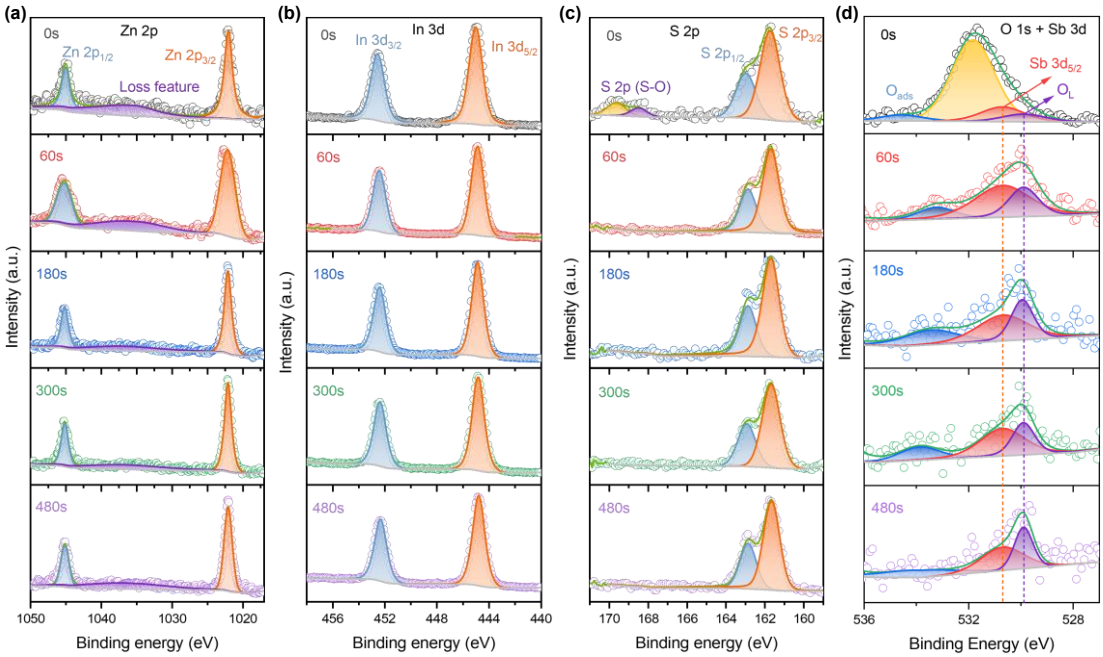

Fig. S20. Fitted core-level spectra of Zn 2*p* (a), In 3*d* (b), S 2*p* (c), and (O1*s* + Sb 3$d_{5/2}$) (d) for the Sb:O-$ZnIn_2S_4$ sample at different XPS depth etching times.

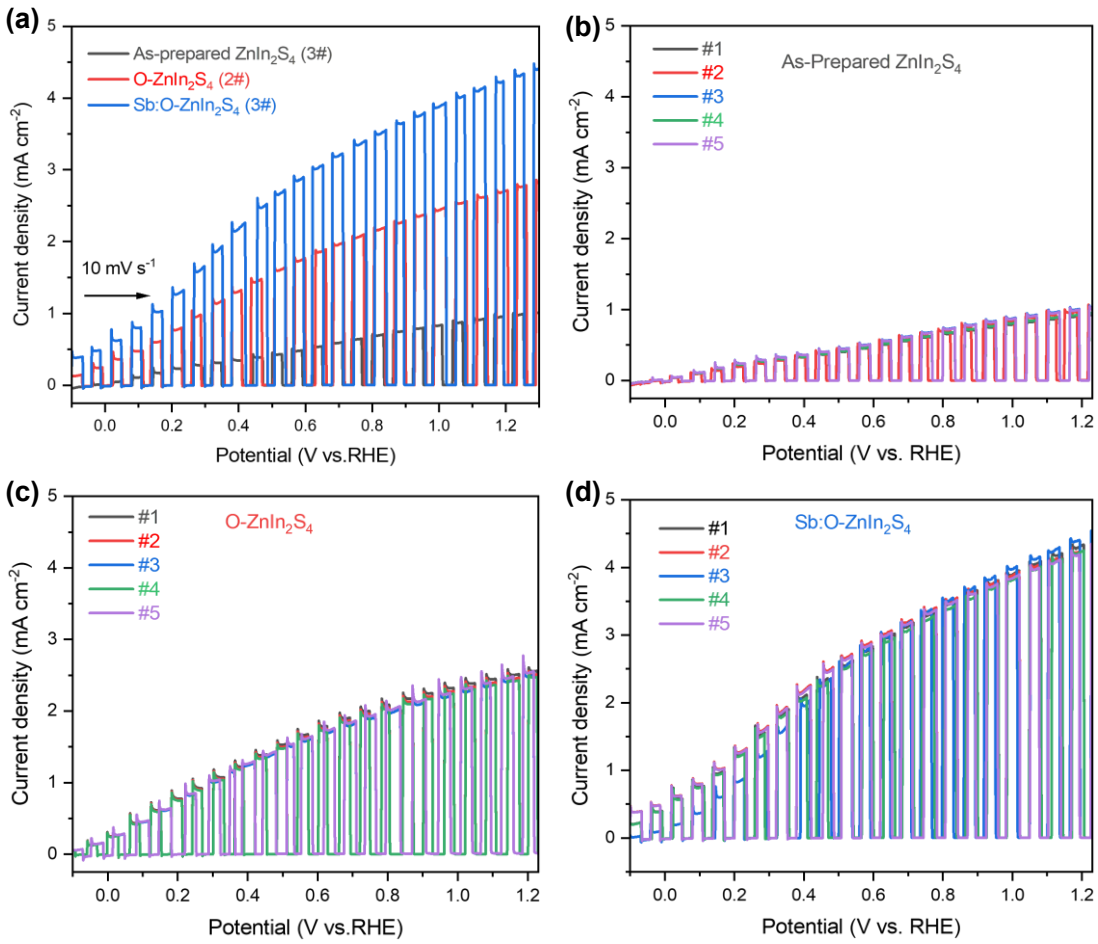

Fig. S21. (a) *J-V* curves of as-prepared $ZnIn_2S_4$ (sample #3 in panel b), O-$ZnIn_2S_4$ (sample #2 in panel c), and Sb:O-$ZnIn_2S_4$ (sample #3 in panel d) photoanodes measured in 0.5M Na_2SO_4 (pH 6.8) under chopped AM1.5G simulated sunlight (100 mW cm^{-2}) with a scan rate of 10 mV s^{-1}. (b-d) Reproducibility of the chopped *J-V* curves measured for five independently prepared electrodes for each sample type, including (b) as-prepared $ZnIn_2S_4$, (c) O-$ZnIn_2S_4$, and (d) Sb:O-$ZnIn_2S_4$ photoanodes.

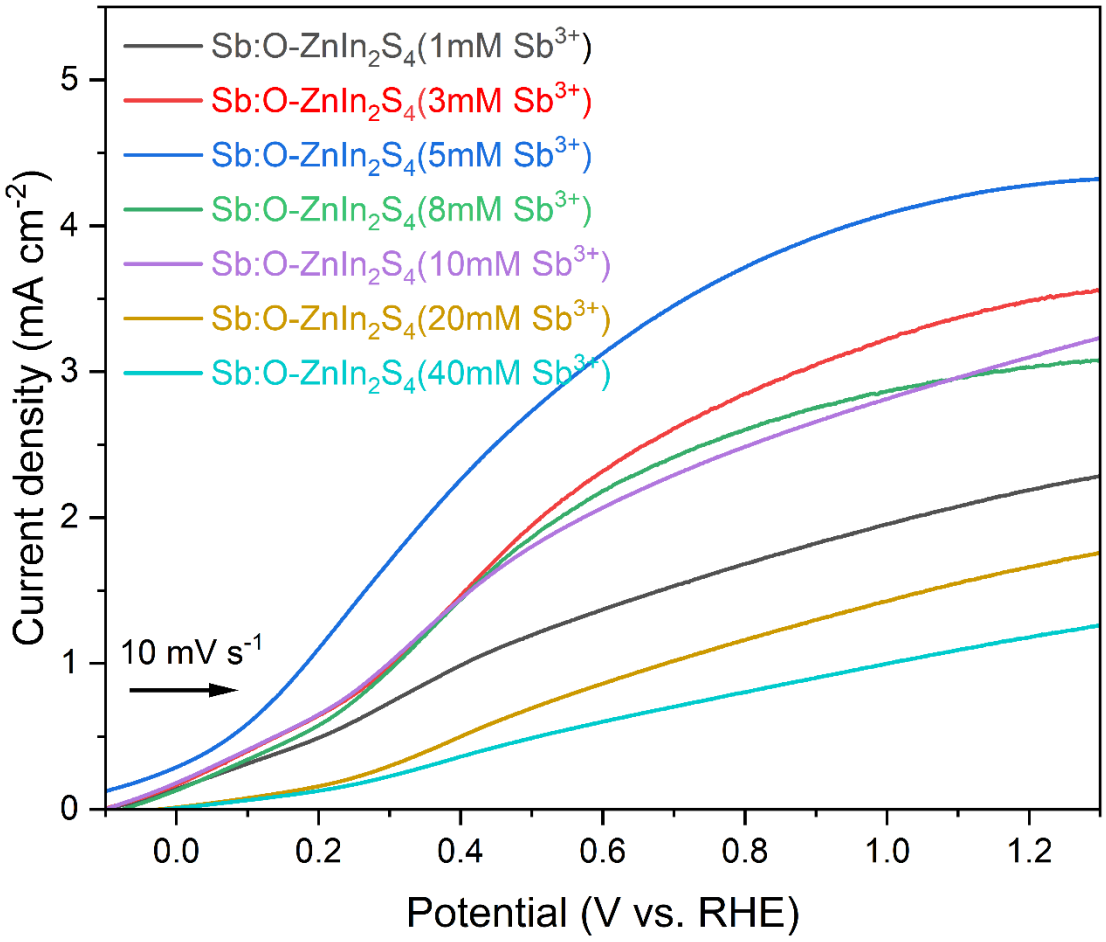

Fig. S22. *J-V* curves for Sb:O-$ZnIn_2S_4$ photoanodes with different Sb incorporation concentrations, measured in 0.5M Na_2SO_4 (pH 6.8) under continuous AM1.5G simulated sunlight (100 mW cm^{-2}) with a scan rate of 10 mV s^{-1}.

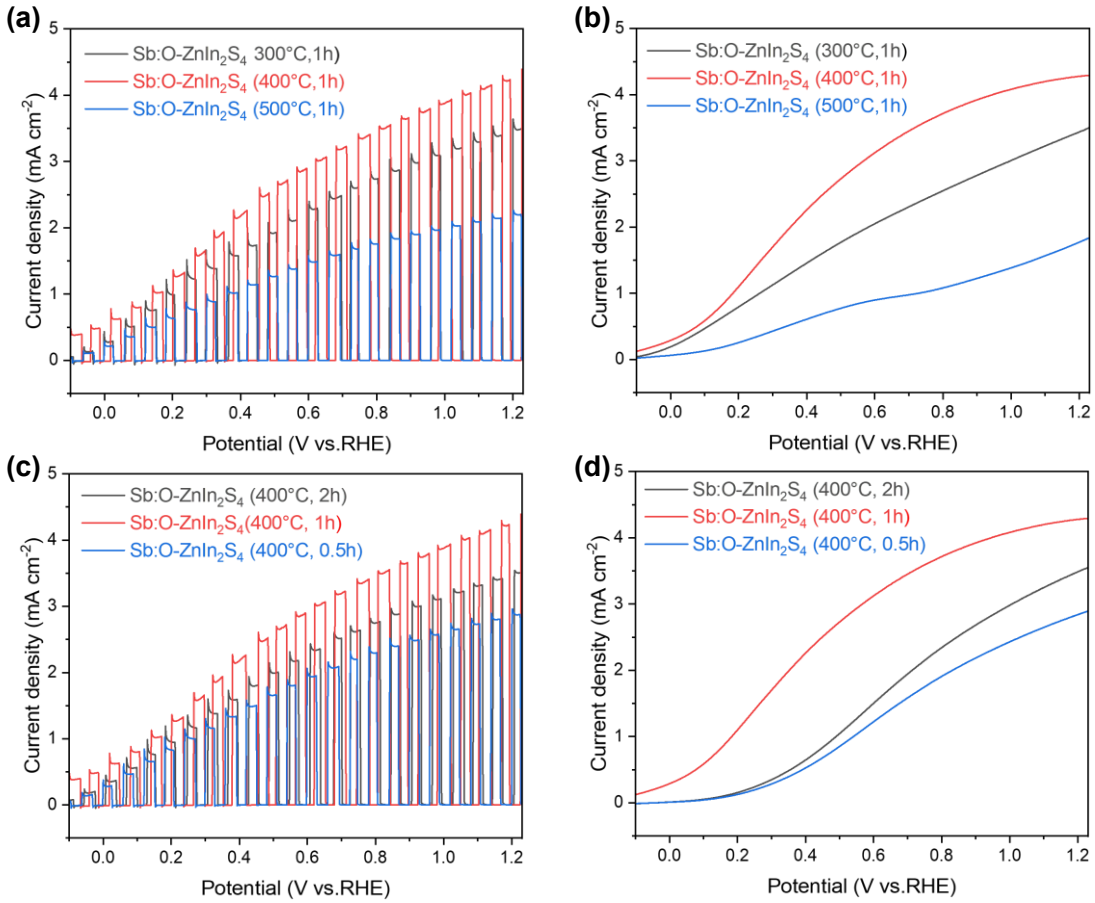

Fig. S23. Annealing temperature and time dependence of the PEC performance of O-$ZnIn_2S_4$ and Sb:O-$ZnIn_2S_4$ photoanodes measured in 0.5 M Na_2SO_4 (pH 6.8) under AM 1.5G illumination (100 mW cm^{-2}). (a, b) *J-V* curves of photoanodes annealed at different temperatures. (c, d) *J-V* curves of photoanodes annealed for different durations. The optimal condition is 400 °C for 1 h. Lower temperature or shorter time results in insufficient lattice O incorporation, whereas higher temperature or longer time leads to excessive surface oxidation, consistent with the increased S-O contribution.

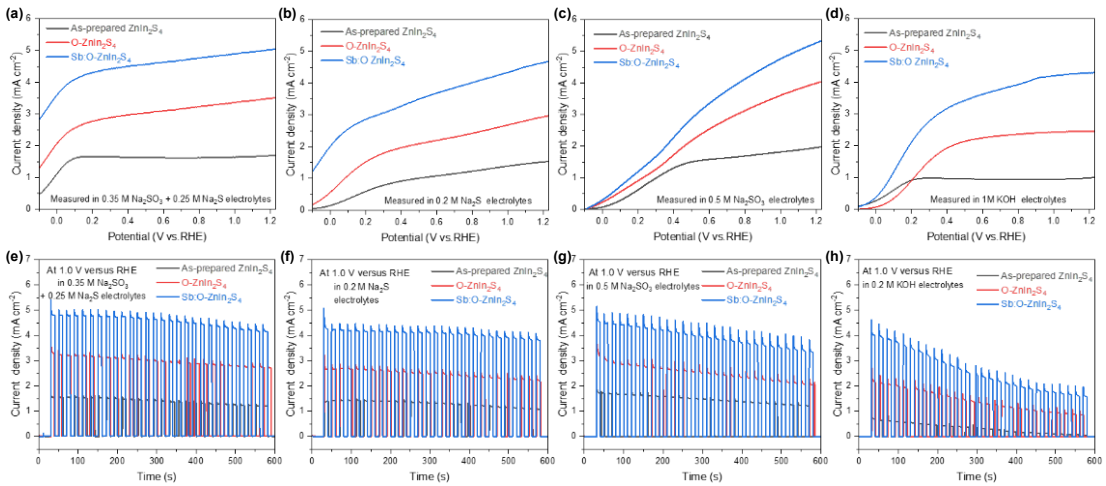

Fig. S24. (a-d) *J-V* curves of as-prepared $ZnIn_2S_4$, O-$ZnIn_2S_4$, and Sb:O-$ZnIn_2S_4$ photoanodes measured under AM1.5G simulated sunlight (100 mW cm^{-2}) in commonly used electrolytes for sulfide-based photoelectrochemical testing, including 0.35 M Na_2SO_3 + 0.25 M Na_2S (pH 13.5) (a), 0.2 M Na_2S (pH 13.0) (b), 0.5 M Na_2SO_3 (pH 9.8) (c), and 1 M KOH (pH 14) (d). (e-h) The corresponding chopped *J-T* curves were recorded in the same electrolytes at 1.0 V versus RHE under AM 1.5G illumination. Across all these electrolytes, the $ZnIn_2S_4$-based photoanodes exhibit the same performance ranking as in neutral Na_2SO_4, namely that O incorporation and subsequent Sb modification systematically enhance the PEC activity. electrolytes containing hole scavengers (Na_2SO_3 and/or Na_2S) generally suppress surface hole accumulation and therefore mitigate oxidative attack on sulfide lattices, often leading to higher apparent photocurrents and improved short-term stability compared with a purely supporting electrolyte. By contrast, strongly alkaline media (KOH) can accelerate surface reconstruction and sulfide oxidation under anodic bias due to stronger nucleophilic/oxidizing conditions. Against this backdrop, the improved behavior of Sb:O-$ZnIn_2S_4$ could be rationalized by our spectroscopic evidence that Sb promotes lattice/near-lattice O incorporation while suppressing the formation of surface oxidized sulfur species.

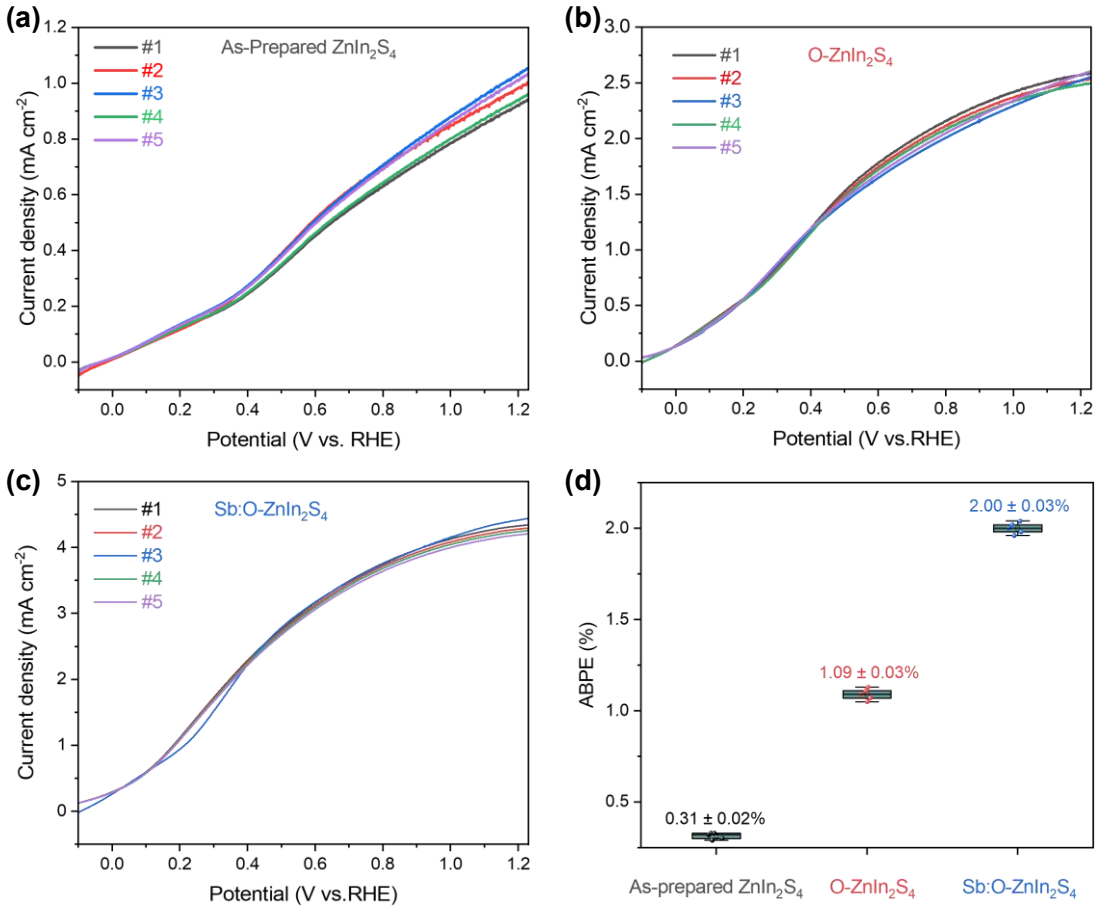

Fig. S25. Reproducibility of the PEC performance of $ZnIn_2S_4$-based photoanodes. (a-c) *J-V* curves for batches of five samples are shown in (a) as-prepared $ZnIn_2S_4$, (b) O-$ZnIn_2S_4$, and (c) Sb:O-$ZnIn_2S_4$ photoanodes. The *J-V* curves for the representative (champion) photoanodes under each condition are reported in **Fig. 5a**. (d) Statistical distribution of the ABPEs for the corresponding photoanodes. The average ABPEs and the standard deviations are shown in the box chart.

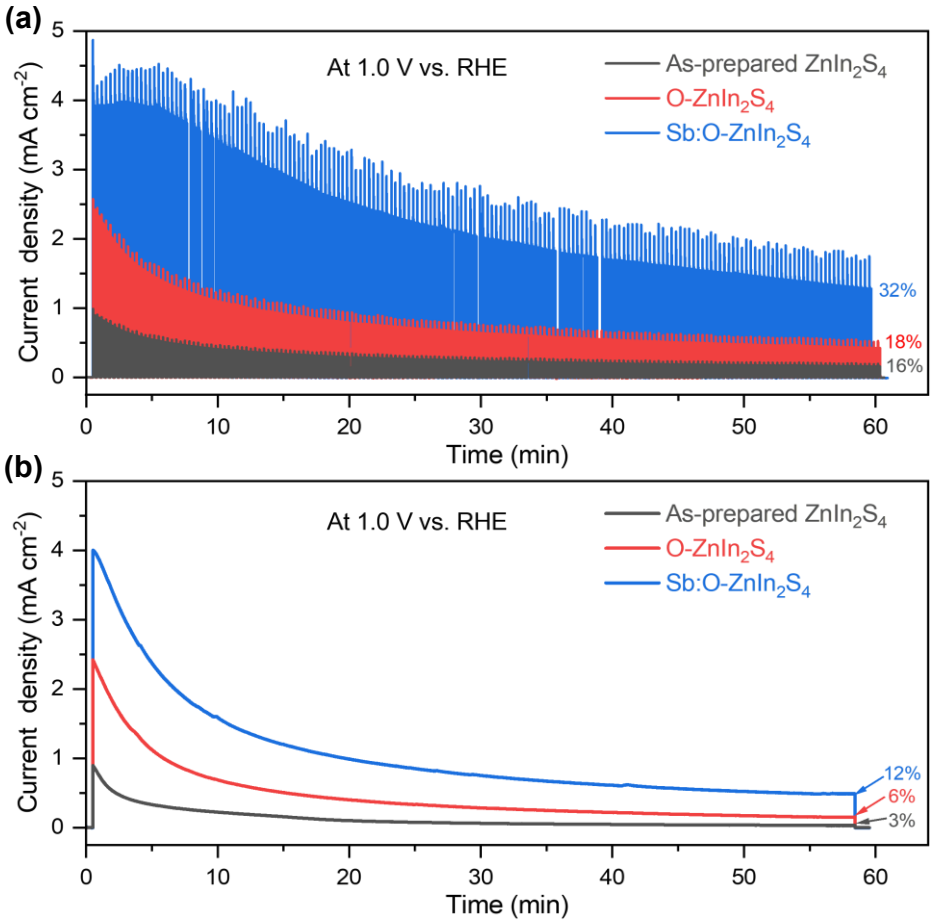

Fig. S26. Extended PEC stability tests of as-prepared $ZnIn_2S_4$, O-$ZnIn_2S_4$, and Sb:O-$ZnIn_2S_4$ photoanodes measured in 0.5 M Na_2SO_4 electrolyte at 1.0 V vs. RHE. *J-T* curves were recorded under chopped (a) and continuous (b) AM 1.5G illumination for 60 min. All photoanodes exhibit noticeable photocurrent decay on the time scale of tens of minutes. Under chopped illumination, the Sb:O-$ZnIn_2S_4$ photoanode retains ~32% of its initial photocurrent after 60 min, compared with ~16% for as-prepared $ZnIn_2S_4$ and ~18% for O-$ZnIn_2S_4$. Under continuous illumination, Sb:O-$ZnIn_2S_4$ maintains ~12% of the initial photocurrent after 60 min, whereas as-prepared $ZnIn_2S_4$ and O-$ZnIn_2S_4$ retain only ~3% and ~6%, respectively. Overall, the Sb:O-$ZnIn_2S_4$ photoanode shows a slower decay rate and higher photocurrent retention than control samples under both illumination modes, indicating an improved resistance to photocorrosion on the same time scale.

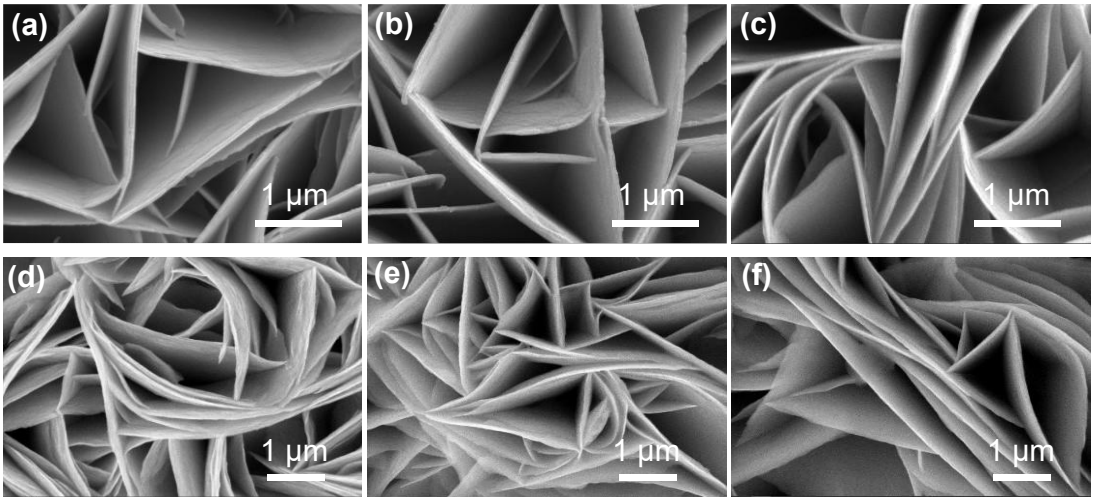

Fig. S27. Top-view SEM images for as-prepared $ZnIn_2S_4$ (a, d), O-$ZnIn_2S_4$ (b, e), and Sb:O-$ZnIn_2S_4$ (c, f) samples before (a-c) and after (d-f) a 10 min PEC test.

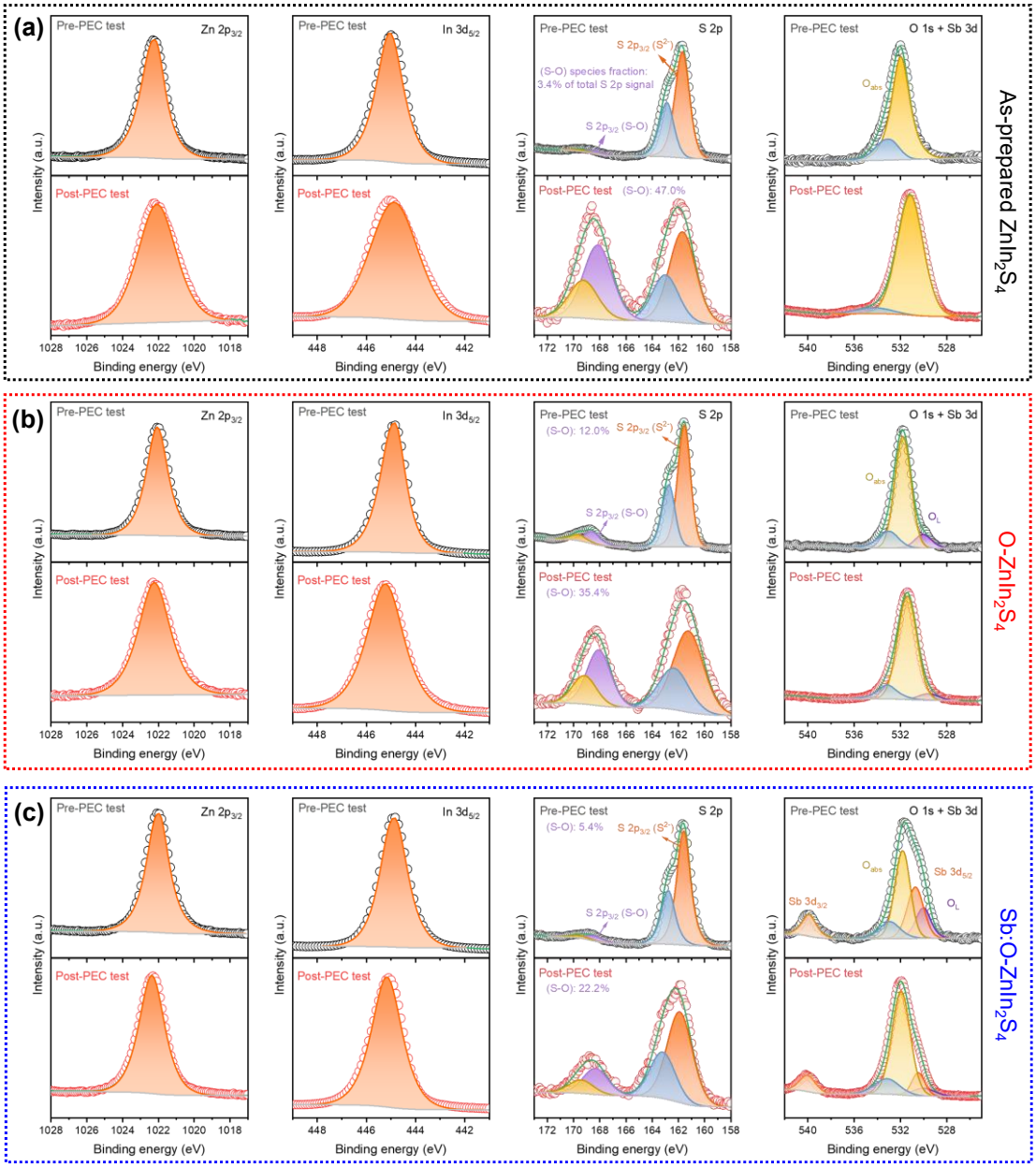

Fig. S28. HAXPES spectra of as-prepared $ZnIn_2S_4$ (a), O-$ZnIn_2S_4$ (b), and Sb:O-$ZnIn_2S_4$ (c) photoanodes recorded before and after a 10 min PEC test. After PEC operation, the chemical states of Zn and In remain essentially unchanged, whereas partial oxidation of sulfur species is detected. The S 2p spectra reveal an increased contribution of S-O species for all samples, with the most pronounced increase for as-prepared $ZnIn_2S_4$, followed by O-$ZnIn_2S_4$. In contrast, Sb:O-$ZnIn_2S_4$ exhibits a markedly lower degree of sulfur oxidation, indicating that Sb incorporation mitigates surface sulfur oxidation under anodic conditions. Notably, lattice-related O 1s components and Sb species remain detectable after PEC testing, suggesting that the Sb-induced O incorporation is not rapidly lost during short-term PEC operation.

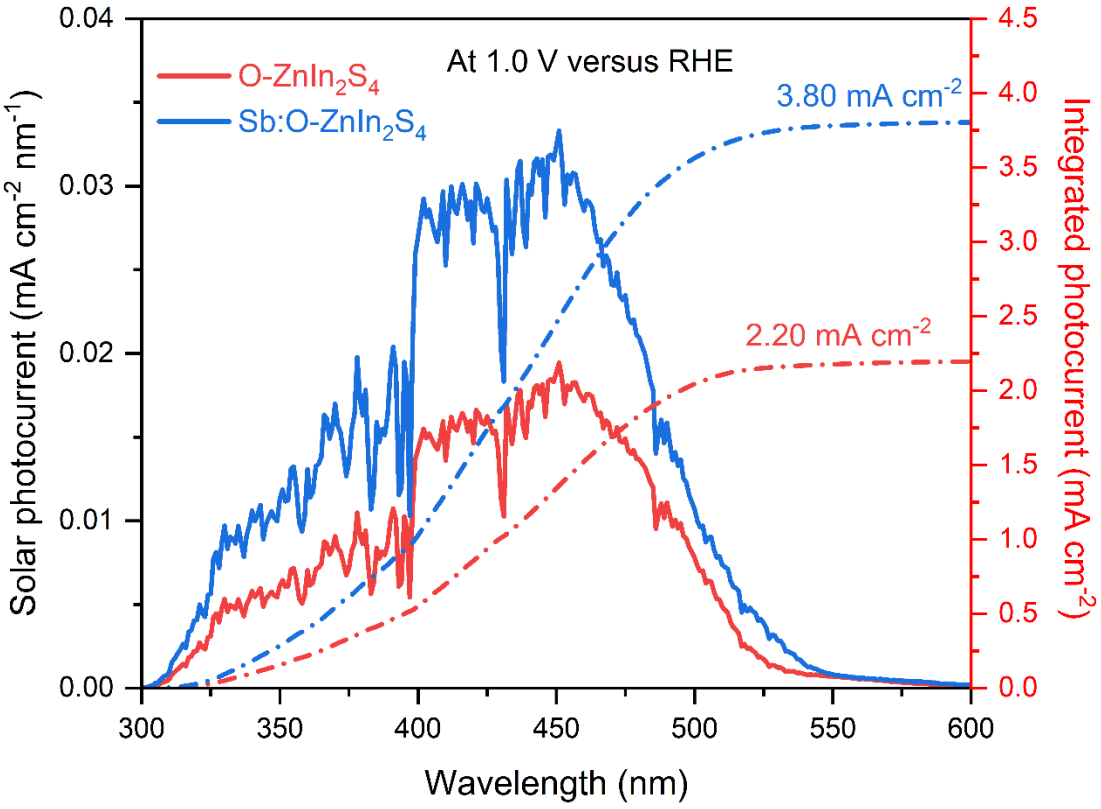

Fig. S29. Solar photocurrent spectra and integrated photocurrent curves for O-$ZnIn_2S_4$ and Sb:O-$ZnIn_2S_4$ photoanodes, calculated by multiplying the IPCE spectra (**Fig. 5d**) with the standard AM 1.5G spectrum (ASTM G173-03).

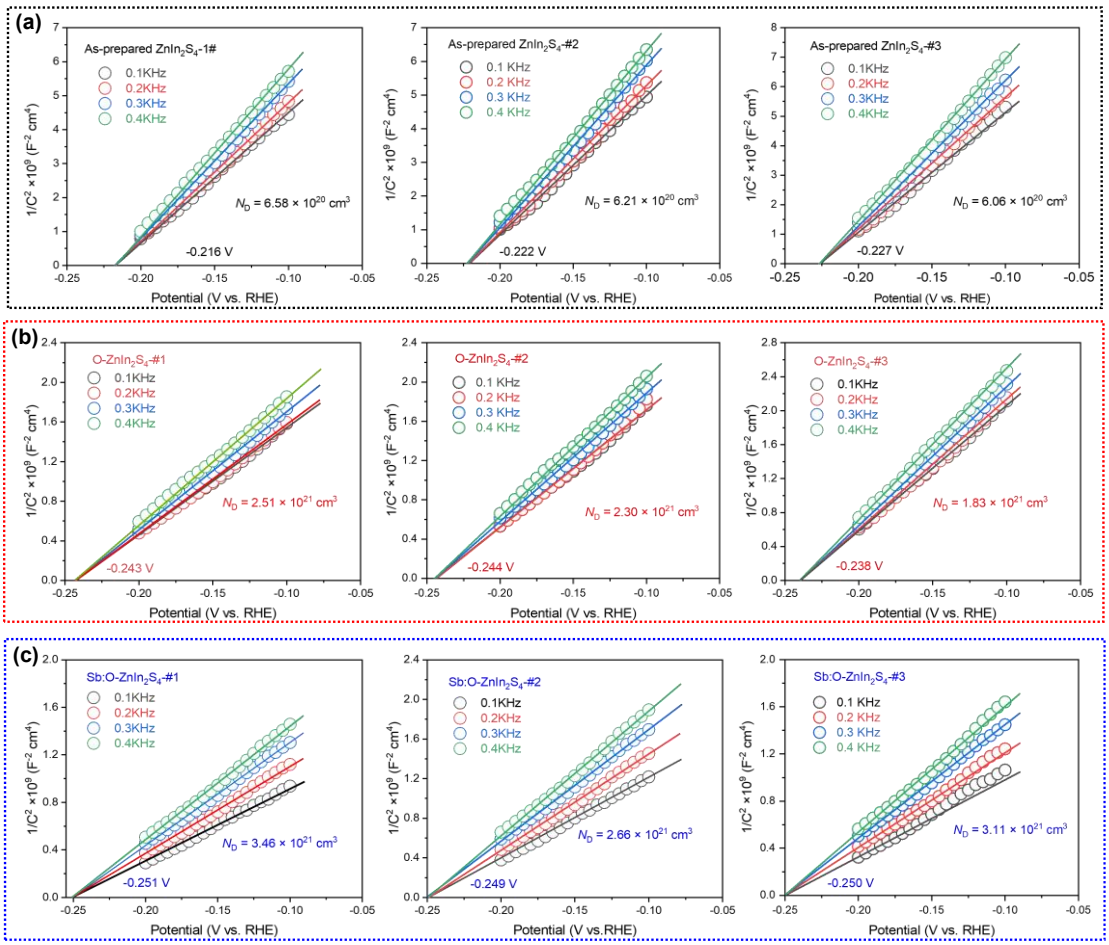

Fig. S30. Mott-Schottky plots of as-prepared $ZnIn_2S_4$ (a), O-$ZnIn_2S_4$ (b), and Sb:O-$ZnIn_2S_4$ (c) photoanodes, measured for three independently prepared samples in 0.5 M Na_2SO_4 electrolyte under dark conditions. The potential was scanned anodically at frequencies of 0.1, 0.2, 0.3, and 0.4 kHz with an AC amplitude of 15 mV. The lines show the fitting of the linear regions of the Mott-Schottky plots. From the interceptions of the lines with the *x*-axis, the flat-band potentials of the samples were obtained. The carrier concentration (N_D) in the samples was estimated from the slope (k_S) of the lines using $N_D = 2/(e\varepsilon_0\varepsilon_r k_S)$, where e is electron charge, ε_0 is vacuum permittivity, and ε_r is the dielectric constant of $ZnIn_2S_4$ (~4.7). At the frequency of 0.3 kHz, the N_D values for as-prepared $ZnIn_2S_4$, O-$ZnIn_2S_4$, and Sb:O-$ZnIn_2S_4$ photoanodes were calculated to be $(6.28 \pm 0.27) \times 10^{20}$ cm^{-3}, $(2.21 \pm 0.35) \times 10^{21}$ cm^{-3}, and $(6.28 \pm 0.27) \times 10^{21}$ cm^{-3}.

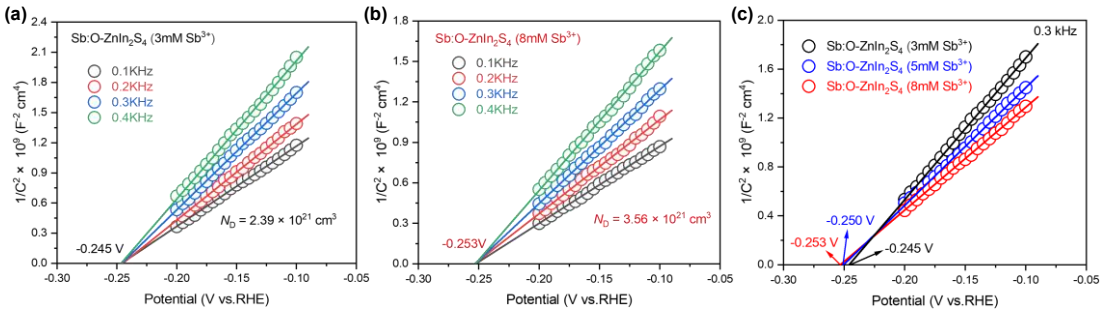

Fig. S31. Mott-Schottky plots of Sb:O-$ZnIn_2S_4$ with varying Sb incorporation concentrations. With increasing Sb content, the flat-band potential gradually shifts cathodically and the N_D increases, which in theory should enhance PEC performance. However, the *J-V* curves in **Fig. S22** show that the PEC performance improves initially but deteriorates at higher Sb concentrations, likely because excessive Sb incorporation introduces defect levels that act as recombination centers, thereby impairing PEC activity.

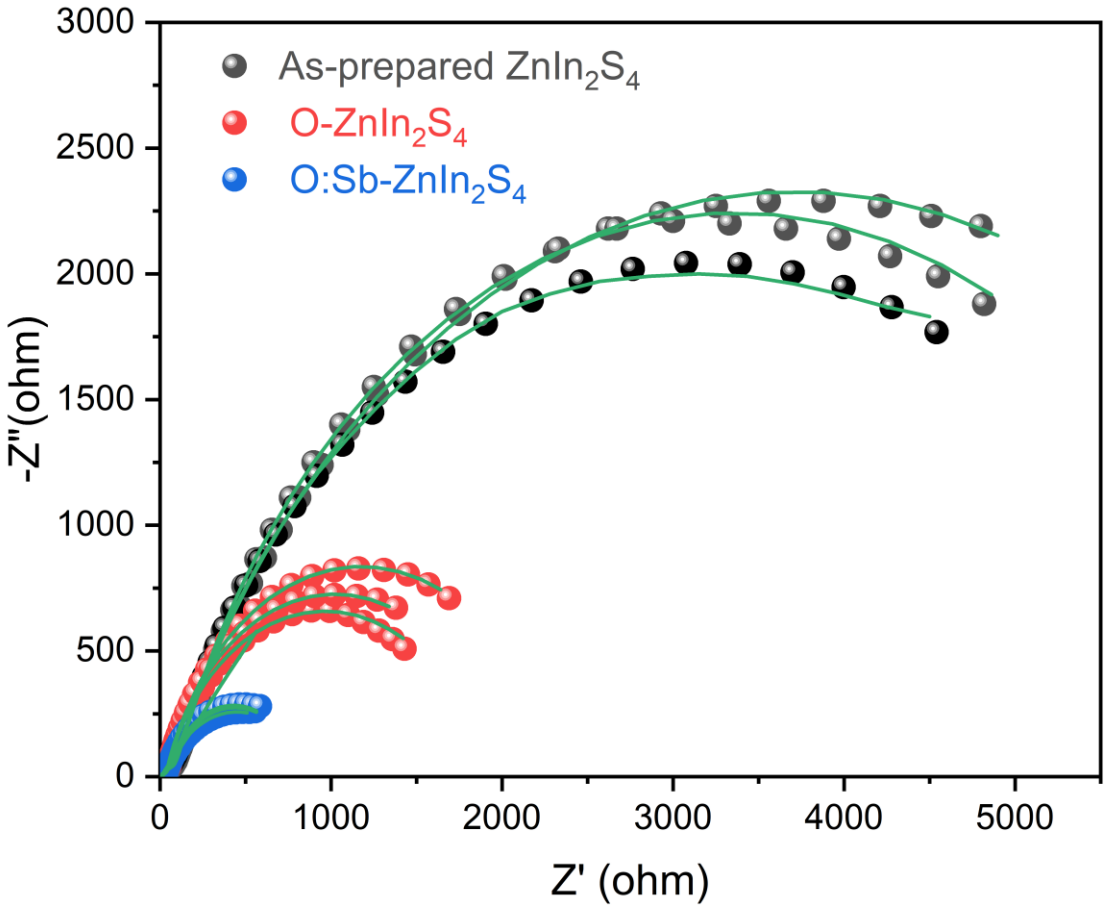

Fig. S32. PEIS for as-prepared $ZnIn_2S_4$, O-$ZnIn_2S_4$, and Sb:O-$ZnIn_2S_4$ photoanodes, measured for three independently prepared samples in 0.5M Na_2SO_4 electrolyte under AM 1.5G simulated sunlight. Green lines represent the fitted the Nyquist plot of the PEIS data using a two-RC-unit equivalent circuit.

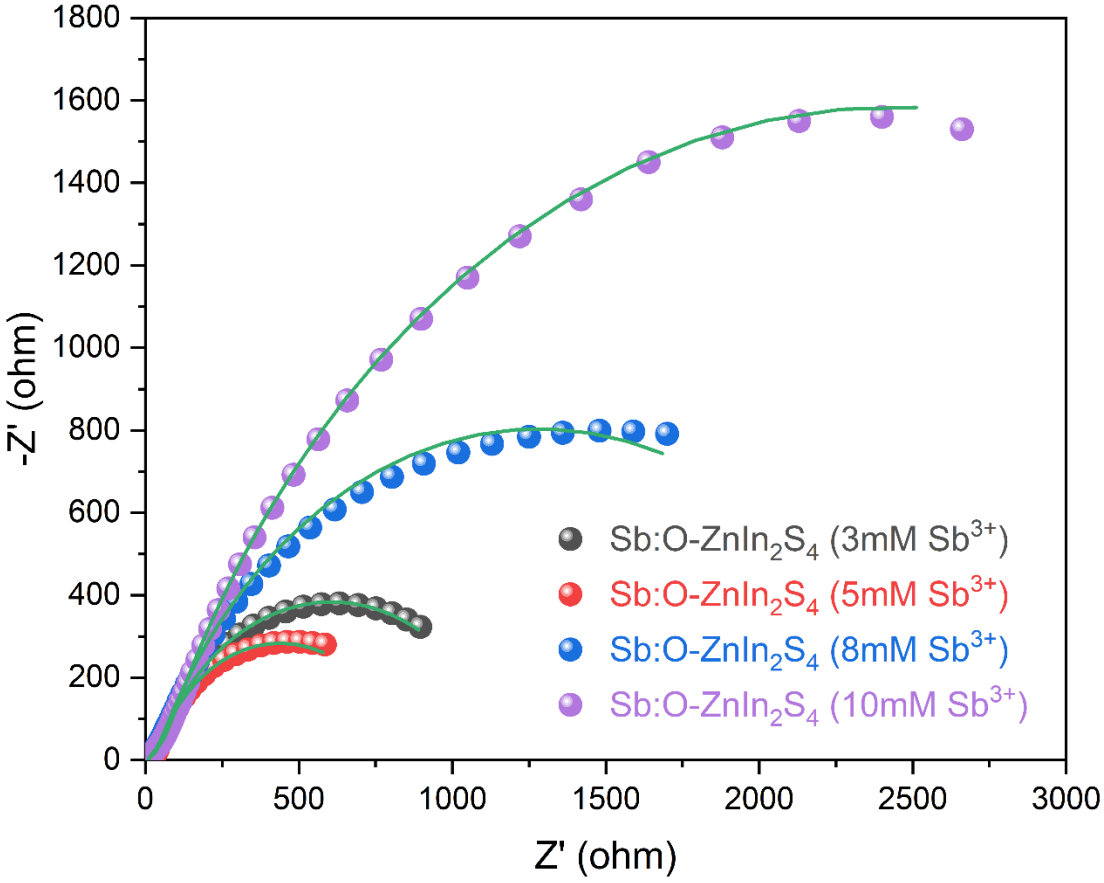

Fig. S33. PEIS for Sb:O-$ZnIn_2S_4$ photoanodes with varying Sb incorporation concentrations measured in 0.5M Na_2SO_4 electrolyte under AM 1.5G simulated sunlight. Green lines represent the fitted the Nyquist plot of the PEIS data using a two-RC-unit equivalent circuit.

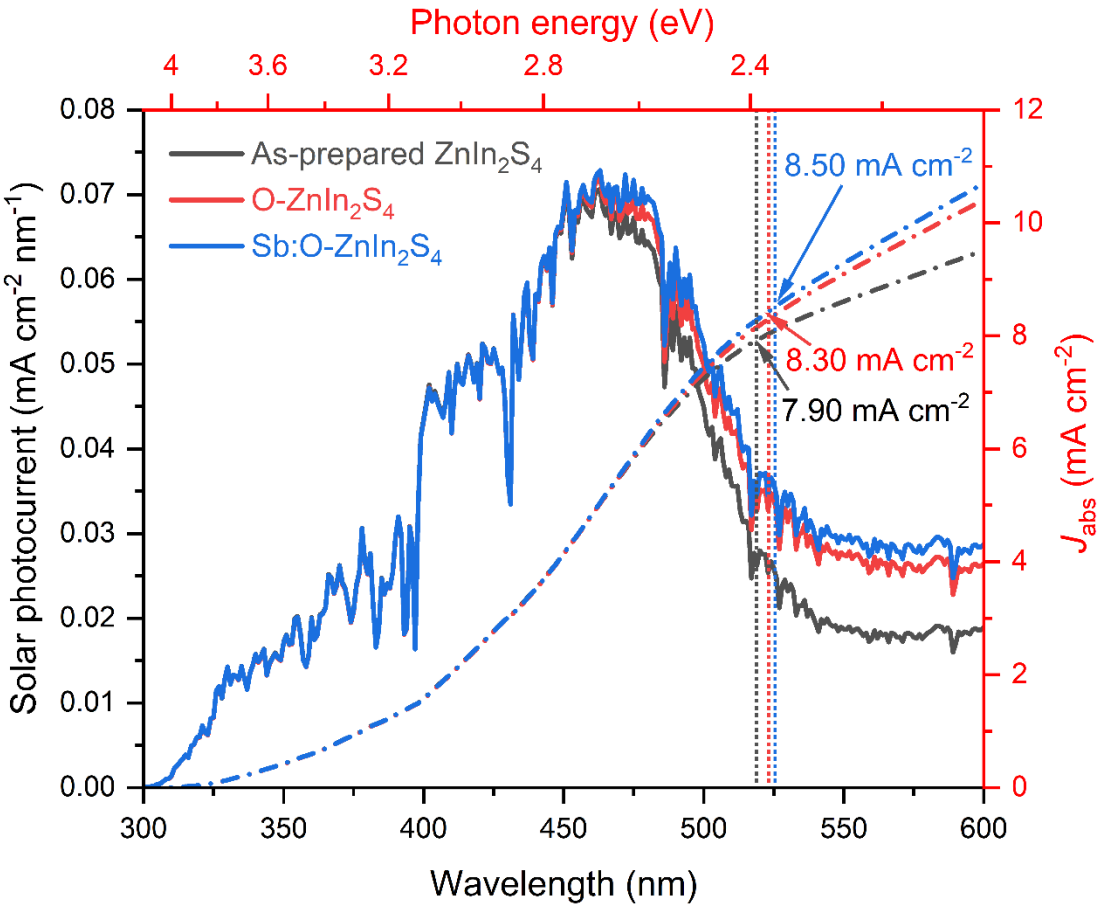

Fig. S34. Absorbed solar photocurrent spectra and absorption photocurrent (J_{abs}) curves for O-$ZnIn_2S_4$ and Sb:O-$ZnIn_2S_4$ photoanodes obtained by integrating the absorption spectra shown in **Fig. 4a** (assuming 100% absorbed photon-to-current conversion efficiency) with the AM 1.5G reference spectrum (ASTM G173-03).

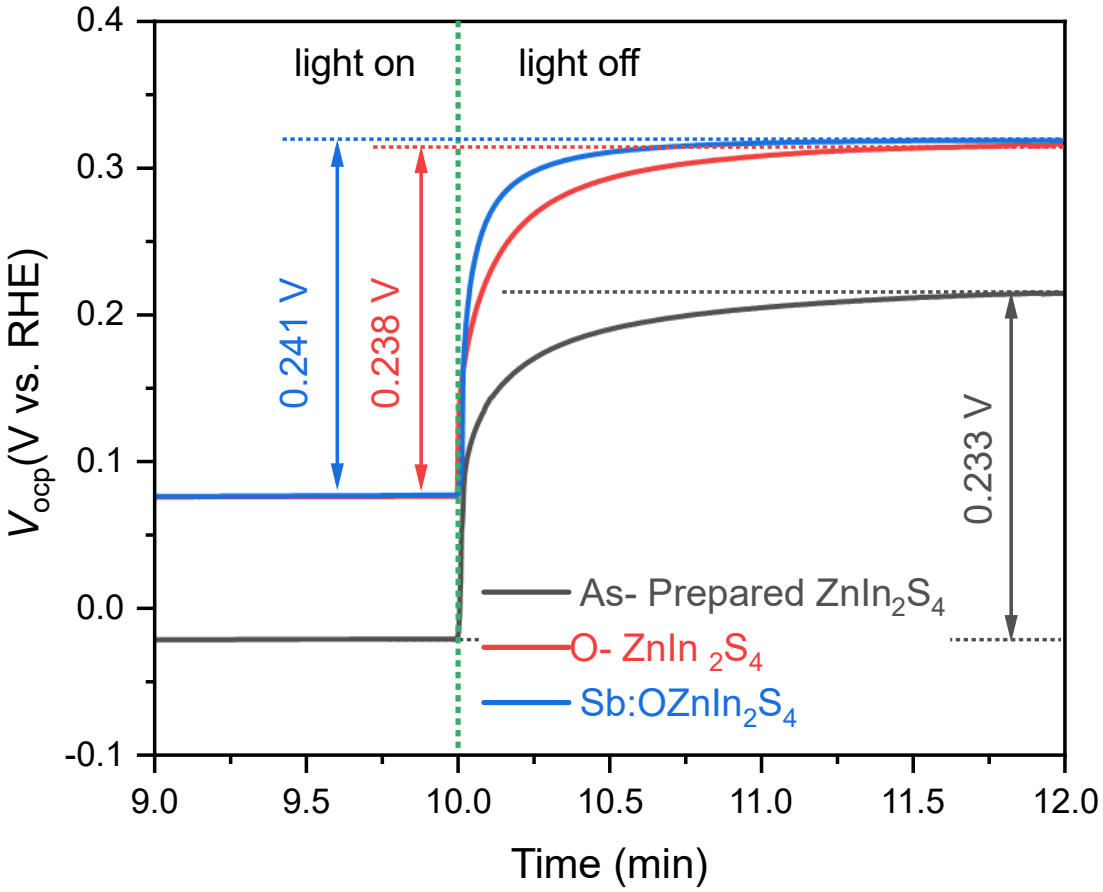

Fig. S35. Open circuit potential (OCP) decay profiles for as-prepared $ZnIn_2S_4$, O-$ZnIn_2S_4$, and Sb:O-$ZnIn_2S_4$ photoanodes under illumination and in the dark. The measurements were conducted in 0.5M Na_2SO_4 electrolyte. After recording the OCP for 10 minutes, the AM 1.5G simulated sunlight was turned off to create significant charge recombination. Carrier lifetimes derived from OCP-decay curves in **Fig. 5i**, were ~0.27 s (as-prepared $ZnIn_2S_4$), ~0.10 s (O-$ZnIn_2S_4$), and ~0.086 s (Sb:O-$ZnIn_2S_4$). The accelerated decay kinetics upon light-off indicate suppressed charge trapping in the Sb:O-$ZnIn_2S_4$, thereby promoting charge separation and enhances PEC activity.

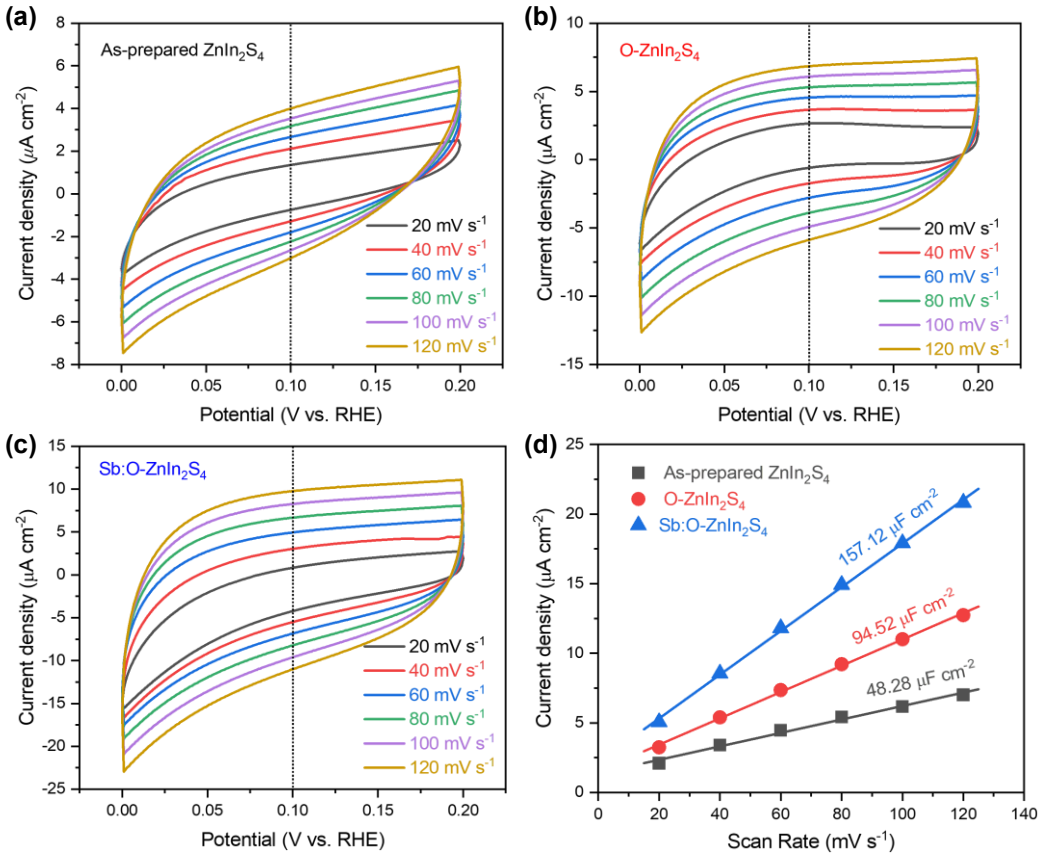

Fig. S36. (a-c) Cyclic voltammograms of as-prepared $ZnIn_2S_4$ (a), O-$ZnIn_2S_4$ (b), and Sb:O-$ZnIn_2S_4$ (c) photoanodes recorded in 0.5 M Na_2SO_4 solution at various scan rates. (d) Difference between the cathodic and anodic charging current densities at 0.10 V vs. RHE plotted as a function of scan rate for the three photoanodes. The slope of the linear fitting corresponds to twice the double-layer capacitance (C_{dl}), which is used to estimate the electrochemically active surface area (ECSA). SEM analysis confirms that the nanosheet morphology is largely preserved after air annealing and subsequent Sb incorporation, indicating that the increased ECSA does not originate from geometric surface area enlargement but from chemical/electronic activation of surface states. O-related surface species introduced during air annealing enhance interfacial charge storage and provide additional adsorption/coordination sites for oxygenated intermediates, facilitating hole accumulation. Subsequent Sb incorporation further regulates these O-related surface species by suppressing sulfur oxidation and stabilizing electronically favorable surface states, as evidenced by increased C_{ss}, reduced R_{ct}, and enhanced η_{inj}. As a result, the enlarged ECSA of Sb:O-$ZnIn_2S_4$ reflects both a higher density of accessible active sites and improved interfacial reaction kinetics.

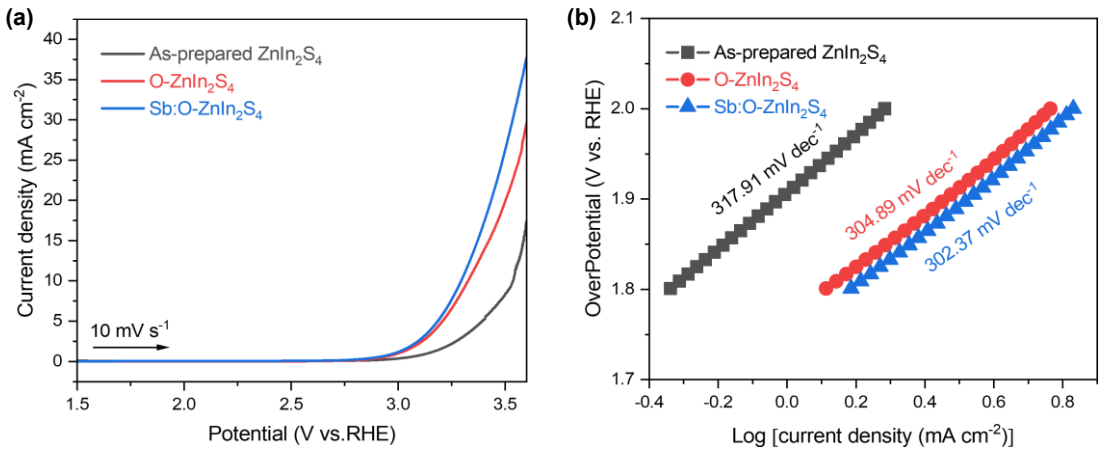

Fig. S37. (a) Dark *J-V* curves of as-prepared $ZnIn_2S_4$, O-$ZnIn_2S_4$, and Sb:O-$ZnIn_2S_4$ photoanodes measured in 0.5M Na_2SO_4 with a scan rate of 10 mV s^{-1}. (b) Corresponding Tafel plots. The progressively reduced Tafel slopes suggest improved interfacial charge-transfer kinetics after air annealing and subsequent Sb incorporation, consistent with the promoted O-related defect modulation and the enhanced PEC activity.

Table S1. Detailed HAXPES and XPS data analyzed using Thermo Fisher Scientific's Avantage software. The atomic ratios of elements in the samples were quantified based on the Zn $2p_{3/2}$, In $3d_{5/2}$, S $2p_{3/2}$, Sb $3d_{5/2}$, and the lattice O component of the O 1s peak. Sensitivity factors and background subtraction were automatically accounted for by the software during the quantification process.

Sample		Zn $2p_{3/2}$		In $3d_{5/2}$		S $2p_{3/2}$				O 1s				Sb $3d_{5/2}$	
		Position	Atomic (%)	Position	Atomic (%)	S^{2-}		S-O		O_{abs}		O_L		Position	Atomic (%)
						Position	Atomic (%)	Position	Atomic (%)	Position	Atomic (%)	Position	Atomic (%)		
As-prepared $ZnIn_2S_4$		1022.2	11.66	445.1	19.67	161.7	44.37	168.4	1.57	531.9 533.0	18.21 4.52	/	/	/	/
O-$ZnIn_2S_4$		1022.1	10.39	444.8	19.36	161.5	33.29	168.5	4.51	531.8 533.0	24.40 4.92	530.0	3.13	/	/
Sb:O-$ZnIn_2S_4$		1022.0	11.57	444.9	22.98	161.6	38.33	168.4	2.19	531.8 533.0	14.66 3.96	530.0	5.15	530.7	1.16
Etching Time	0 s	1022.0	8.22	445.0	16.40	161.7	26.36	168.5	2.12	531.8 534.0	39.37 2.95	529.0	3.71	530.7	0.87
	60 s	1022.1	14.38	444.9	28.30	161.7	47.78	/	/	533.3	2.75	529.9	5.46	530.7	1.33
	180 s	1022.1	14.33	444.9	28.13	161.7	47.71	/	/	533.4	3.96	529.9	4.95	530.7	0.92
	360 s	1022.1	15.13	444.8	29.78	161.7	50.67	/	/	/	/	529.9	3.67	530.7	0.75
	480 s	1022.1	15.14	444.8	30.12	161.7	51.00	/	/	/	/	529.9	3.22	530.7	0.52

Table S2. Quantitative elemental compositions of the samples obtained from HAXPES and XPS data analysis.

Sample		Atomic ratios							
		In/Zn	**S/Zn**	**[S+(S-O)]/Zn**	**(S-O)/[S+(S+O)]**	**$O_L/(O_{abs}+O_L)$**	**$O_L/[S+O_L]$**	**[S+ (S-O)+O_L]/Zn**	**Sb/[Sb+In]**
As-prepared $ZnIn_2S_4$		1.69	3.80	3.94	0.034	0.00	/	3.94	/
O- $ZnIn_2S_4$		1.86	3.20	3.64	0.12	0.096	0.086	3.94	/
Sb:O-$ZnIn_2S_4$		1.99	3.32	3.50	0.054	0.22	0.12	3.95	0.048
Etching Time	0 s	1.99	3.20	3.47	0.074	0.081	0.12	3.92	0.050
	60 s	1.97	3.32	3.32	0	0.67	0.10	3.70	0.045
	180 s	1.96	3.33	3.38	0	0.56	0.094	3.67	0.032
	360 s	1.97	3.35	3.35	0	1	0.068	3.59	0.025
	480 s	1.99	3.37	3.37	0	1	0.059	3.58	0.017

Table S3. Fitted parameters for the TRPL decay of different Sb:O-$ZnIn_2S_4$ samples. The f_1, f_2, and f_3 are the fractional intensities; τ_1, τ_2, and τ_3 are the lifetimes; τ_{AV} is the intensity-weighted average lifetime, which is equal to $f_1\tau_1 + f_2\tau_2 + f_3\tau_3$; and χ^2 is the reduced chi-square value.

Sample	τ_1 (μs)	f_1	τ_2 (μs)	f_2	τ_3 (μs)	f_3	τ_{AV} (μs)	χ^2
Sb:O-$ZnIn_2S_4$ (3mM $SbCl_3$)	0.18	6.9%	1.24	22.4%	10.22	70.8%	7.52	1.313
Sb:O-$ZnIn_2S_4$ (5mM $SbCl_3$)	0.14	4.1%	1.21	15.6%	12.38	80.4%	10.15	1.823
Sb:O-$ZnIn_2S_4$ (8mM $SbCl_3$)	0.16	8.8%	1.13	25.0%	9.73	66.3%	6.74	1.351

Table S4. Direction-dependent effective masses of electrons and holes for as-prepared $ZnIn_2S_4$, O-$ZnIn_2S_4$, and Sb:O-$ZnIn_2S_4$ calculated at the band edges of the Brillouin zone and reported in units of the free-electron mass (m_0). The electron effective masses (m_e*) and hole effective masses (m_h*) were obtained by parabolic fitting of the CBM and the VBM dispersions shown in **Fig. 3g-i**, respectively, using $m^* = \hbar^2[\partial^2E(k)/\partial k^2]^{-1}$,[1] where $\hbar$ is the reduced Planck constant, k is the wave vector, and $E(k)$ are the energy of the electron at k.

Sample	Electron (m_e*)		Hole (m_h*)		
	Γ → M	Γ → K	Γ→ M	Γ → K	M → K
As-prepared $ZnIn_2S_4$	0.08	0.06	0.28	0.29	/
O-$ZnIn_2S_4$	0.10	0.07	0.72	/	2.18
Sb:O-$ZnIn_2S_4$	0.23	0.26	0.14	0.12	/

Table S5. Total energies, corresponding formation energies (E_{form}) and atomic ratios of the DFT-optimized structural models

Sample	System	Atomic ratios	Model	Total energy (eV)	E_{form} (eV)
As-prepared $ZnIn_2S_4$	O	–	–	-4.938941195	–
	S	–	–	-4.09156015125	–
	Monolayer $ZnIn_2S_4$	–	–	-254.46214984	–
	Monolayer $ZnIn_2S_4$	(In vacancy)/(In atom) = 0.1111	–	-242.09592033	–
O-$ZnIn_2S_4$	O-$ZnIn_{2-x}S_{4-y}$	O/(S+O) = 0.0278	**Model 1**	**-244.01293255**	**-1.06963117625**
			Model 2	-243.68554889	-0.74224751625
			Model 3	-243.79843522	-0.85513384625
	2O-$ZnIn_{2-x}S_{4-y}$	O/(S+O) = 0.0556	Model 1	-245.59202831	-1.8013458925
			Model 2	-245.70489018	-1.9142077625
			Model 3	-245.73717717	-1.9464947525
			Model 4	**-245.83417888**	**-2.0434964625**

	3O-$ZnIn_{2-x}S_{4-y}$	**O/(S+O) = 0.0833**	Model 1	-247.58591166	-2.94784819875
			Model 2	-247.55596800	-2.91790453875
			Model 3	-247.53594780	-2.89788433875
			Model 4	**-247.67108386**	**-3.03302039875**
Sb:O-$ZnIn_2S_4$	Sb-$ZnIn_{2-x}S_{4-y}$	Sb/(Sb + In) =0.058 (In vacancy)/(In + Sb) = 0.0556	–	-249.26941755	–
	Sb:O-$ZnIn_{2-x}S_{4-y}$	Sb/(Sb + In) =0.058 (In vacancy)/(In + Sb) = 0.0556 O/(S+O) = 0.0278	Model 1	-251.14319366	-1.02639506625
			Model 2	-251.41535738	-1.29855878625
			Model 3	**-251.58192351**	**-1.46512491625**
	Sb:2O-$ZnIn_{2-x}S_{4-y}$	Sb/(Sb + In) =0.058 (In vacancy)/(In + Sb) = 0.0556 O/(S+O) = 0.0556	Model 1	-253.67024087	-2.7060612325
			Model 2	-253.36013253	-2.3959528925
			Model 3	**-253.82141074**	**-2.8572311025**
			Model 4	-253.48723374	-2.5230541025

	Sb:3O- $ZnIn_{2-x}S_{4-y}$	Sb/(Sb + In) =0.058 (In vacancy)/(In + Sb) = 0.0556 O/(S+O) = 0.0833	**Model 1**	**-255.84976218**	**-4.03820149875**
			Model 2	-255.49665738	-3.68509669875
			Model 3	-255.66091664	-3.84935595875
			Model 4	-255.57791935	-3.76635866875
	Sb:4O- $ZnIn_{2-x}S_{4-y}$	Sb/(Sb + In) =0.058 V_{In}/(In + Sb) = 0.0556 **O/(S+O) = 0.1111**	Model 1	-257.36352856	-4.704586835
			Model 2	-257.62890228	-4.969960555
			Model 3	**-257.70546358**	**-5.046521855**
			Model 4	-257.65246262	-4.993520895

Table S6. Bandgap and band positions of different $ZnIn_2S_4$ samples determined by UPS spectra and UV-vis absorption spectra.

Sample	E_{BG} **(eV)**	E_F **(eV) vs.** E_{vac}	E_{VB} **(eV) vs.** E_{vac}	E_{CB} **(eV) vs.** E_{vac}
As-prepared $ZnIn_2S_4$	2.39	-4.04	-6.09	-3.70
O-$ZnIn_2S_4$	2.37	-3.94	-6.06	-3.69
Sb:O-$ZnIn_2S_4$	2.36	-3.72	-5.89	-3.53
Sb:O-$ZnIn_2S_4$ (inside)	~2.36	-3.87	-6.04	-3.68

Table S7. PEC water oxidation performances of recently reported $ZnIn_2S_4$-based photoanodes (2014-2025).

Structure	Synthesis method	Photocurrent (mA cm^{-2} at 1.23 V vs. RHE)	HC-STH	Electrolyte	Ref.
$ZnIn_2S_4$ (O_V, SO_4^{2-})	Hydrothermal + Na_2S treatment	3.52	1.7%	NaH_2PO_4/Na_2HPO_4	10
$ZnIn_2S_4$/CdS/ZnO	Hydrothermal + ALD	3.48	1.42%	Na_2SO_4	11
$ZnIn_2S_4/Cu_2S$/ NiFe-LDH	Hydrothermal + ion exchange	1.56	0.224%	Na_2SO_4	12
TiO_2/Cu-$ZnIn_2S_4$	Secondary hydrothermal	2.87	0.51%	Na_2S	13
Pt/$ZnIn_2S_4$/Co-Pi	Hydrothermal + electrochemical deposition	0.91	0.39%	Na_2SO_3/Na_2S	14
$In_2S_3/ZnIn_2S_4$	Hydrothermal	1.22	0.56%	Na_2SO_4	15
Mg:$ZnIn_2S_4$/Co:$ZnIn_2S_4$	Hydrothermal	0.92	0.129%	Na_2SO_4	16
$MoS_2/ZnIn_2S_4$/NiFeOOH	Hydrothermal + photo-deposition	0.74	0.093%	Na_2SO_4	17
$ZnIn_2S_4/Cu_2O$/NiFeOOH/Ag	Hydrothermal + electrochemical deposition + chemical deposition+ chemical water bath	1.22	0.21%	Na_2SO_4	18
$ZnIn_2S_4$ homojunction	Hydrothermal	0.53	0.035%	Na_2S/Na_2SO_3	19
$ZnIn_2S_4$/Au/PB	Hydrothermal + photo-deposition + electrochemical deposition	0.42	Not reported	Na_2SO_4	20
$Sb_2S_3/ZnIn_2S_4/Cu_2S$	Hydrothermal + immersion	2.81	0.744%	Na_2SO_4	21
$Fe_2O_3/Ti_2C_3T_x/ZnIn_2S_4$	Hydrothermal + spin-coating	2.62	0.87%	Na_2SO_4	22

Au-$ZnIn_2S_4$	Hydrothermal + electrochemical deposition	0.52	0.26%	Na_2SO_4	23
$ZnIn_2S_4/SnS_2$	Hydrothermal + ALD	4.57	1.67%	Na_2SO_4	24
Mg:O-$ZnIn_2S_4$	Hydrothermal + low-temperature water bath	4.91	1.61%	Na_2SO_4	25
$ZnIn_2S_4$/Fe-In-S	Hydrothermal + ALD	5.35	1.41%	Na_2SO_4	26
$ZnIn_2S_4$-CoNiP	Hydrothermal	4.77	0.82%	Na_2SO_4	27
$ZnIn_2S_4$/P-$ZnIn_2S_4$	Hydrothermal + Ar annealing	6.34	0.65%	Na_2SO_4	28
S_v-ZIS/N-TiO_2	Hydrothermal	4.77	0.48%	Na_2SO_4	29
$ZnIn_2S_4/TiO_2$	spin coating + electrodeposition	0.8 at 0.5 V vs. Ag/AgCl	Not reported	Na_2SO_4	30
Ni-$ZnIn_2S_4$	Hydrothermal	0.25 at 0.9 V vs. Ag/AgCl	0.014%	Na_2SO_4	31
$SiO_2/ZnIn_2S_4/TiO_2$	Hydrothermal	0.786 at 0.1 V vs. Ag/AgCl	0.48%	Na_2S/Na_2SO_3	32
$Ni(OH)_2$/CdS/$ZnIn_2S_4/TiO_2$	Hydrothermal + immersion	1.8 at 0.1 V vs. Ag/AgCl	0.93%	Na_2S/Na_2SO_3	33
$ZnIn_2S_4/TiO_2$	Hydrothermal	1.2 at 1.5 V vs. RHE	0.96%	Na_2S/Na_2SO_3	34
ZnO/RGO/$ZnIn_2S_4$	Hydrothermal	1.43 at 0.5 V vs. Ag/AgCl	0.46%	Na_2SO_4	35
TiO_2/Cd-doped $ZnIn_2S_4$	two-stage anodization approach + Hydrothermal	606.2 μA cm^{-2}	0.38%	Na_2SO_4	36
O:V_{Zn}:V_S-$ZnIn_2S_4/Al_2O_3$	Hydrothermal + ALD	4.63	Not reported	Na_2SO_3	37
Sb:O-$ZnIn_2S_4$	**Hydrothermal**	**4.30**	**2.00%**	**Na_2SO_4**	**This work**

Table S8. Fitted values of CPE parameters (including magnitude parameter Y_0 and exponent n representing the degree of deviation from ideal capacitive behavior), resistances (R_s, R_{trap}, and R_{ct}), and effective capacitance (C) obtained from EIS measurements.

Sample	R_s (Ω cm^2)	CPE$_{bulk}$			R_{trap} (Ω cm^2)	CPE$_{ss}$			R_{ct} (Ω cm^2)	$\frac{R_{trap}}{R_{trap}+R_{ct}}$
		$Y_{0,1}$ (Ω^{-1} cm^{-2} s^n)	n_1	C_{bulk} (μF cm^{-2})		$Y_{0,2}$ (Ω^{-1} cm^{-2} s^n)	n_2	C_{ss} (μF cm^{-2})		
As-prepared $ZnIn_2S_4$	3.94 ± 0.47	(1.64 ± 6.22)×10^{-4}	0.67 ± 0.01	4.41 ± 1.76	56.74 ± 25.71	(6.78 ± 1.87) ×10^{-5}	0.80 ± 0.03	27.62 ± 11.21	2133.15 ± 639.84	0.025 ± 0.004
O-$ZnIn_2S_4$	3.44 ± 0.63	(8.53 ± 2.01)×10^{-5}	0.72 ± 0.03	4.42 ± 0.96	18.53 ± 9.55	(1.16 ± 1.47)×10^{-4}	0.85 ± 0.02	38.24 ± 3.77	626.03 ± 113.14	0.029 ± 0.017
Sb:O-$ZnIn_2S_4$ (5mM $SbCl_3$)	**2.67 ± 0.46**	**(4.20 ± 3.20)×10^{-5}**	**0.76 ± 0.07**	**5.78 ± 0.69**	**9.32 ± 2.25**	**(3.32 ± 1.15)×10^{-4}**	**0.74 ± 0.07**	**58.22 ± 3.29**	**225.59 ± 5.34**	**0.040 ± 0.007**
Sb:O-$ZnIn_2S_4$ (3mM $SbCl_3$)	2.77	9.58×10^{-5}	0.74	5.29	9.54	3.24×10^{-4}	0.75	46.75	326.33	`0.028
Sb:O-$ZnIn_2S_4$ (8mM $SbCl_3$)	3.39	1.85×10^{-4}	0.68	5.74	25.63	1.01×10^{-4}	0.78	18.65	761.05	0.033
Sb:O-$ZnIn_2S_4$ (10mM $SbCl_3$)	3.42	9.19×10^{-5}	0.71	3.41	29.12	1.00×10^{-4}	0.77	17.37	1469.71	0.019

Supplementary References

1 G. Kresse and J. Furthmuller, *Phys. Rev. B*, 1996, **54**, 11169.

2 G. Kresse and J. Furthmuller, *Comput. Mater. Sci.*, 1996, **6**, 15-50.

3 G. Kresse and D. Joubert, *Phys. Rev. B*, 1999, **59**, 1758.

4 K. B. John P. Perdew and M. Ernzerhof, *Phys. Rev. B*, 1996, **77**, 3865.

5 K. Lee, É. D. Murray, L. Kong, B. I. Lundqvist and D. C. Langreth, *Phys. Rev. B*, 2010, **82**, 081101.

6 Y. Xiao, J. Fu, Y. Pihosh, K. Karmakar, B. Zhang, K. Domen and Y. Li, *Chem. Soc. Rev.*, 2025, **54**, 1268-1317.

7 P. Wang, Z. Shen, Y. Xia, H. Wang, L. Zheng, W. Xi and S. Zhan, *Adv. Funct. Mater.*, 2018, **29**, 1807013.

8 A. Zaban, M. Greenshtein and J. Bisquert, *ChemPhysChem*, 2003, **4**, 859-864.

9 H. Wang, Y. Xia, H. Li, X. Wang, Y. Yu, X. Jiao and D. Chen, *Nat. Commun.*, 2020, **11**, 3078.

10 W. Xu, W. Gao, L. Meng, W. Tian and L. Li, *Adv. Energy Mater.*, 2021, **11**, 2101181.

11 W. Xu, W. Tian, L. Meng, F. Cao and L. Li, *Adv. Energy Mater.*, 2021, **11**, 2003500.

12 Z. Hao, R. Wang, L. Zhang, H. Sheng, Y. Li, B. Dong and L. Cao, *Chem. Eng. J.*, 2023, **468**, 143568.

13 G. Wang, X. Sun, C. Xia, H. Li, B. Dong and L. Cao, *Colloids Surf. A*, 2024, **689**, 133656.

14 M. Zhou, Z. Liu, Q. Song, X. Li, B. Chen and Z. Liu, *Appl. Catal. Environ.*, 2019, **244**, 188-196.

15 H. Geng, P. Ying, K. Li, Y. Zhao and X. Gu, *Appl. Surf. Sci.*, 2021, **563**, 150289.

16 H. Qian, Z. Liu, J. Ya, Y. Xin, J. Ma and X. Wu, *J. Alloys Compd.*, 2021, **867**, 159028.

17 H. Qian, Z. Liu, B. Zhang, J. Li and J. Ya, *ChemCatChem*, 2021, **13**, 1940-1950.

18 Z. Hu, R. Wang, C. Han and R. Chen, *J. Colloid Interface Sci.*, 2022, **628**, 946-954.

19 H. Qian, Z. Liu, Z. Guo, M. Ruan and J. Ma, *J. Alloys Compd.*, 2020, **830**, 154639.

20 L. Wang, M. Zheng, L. Lai, R. Wang, T. Qian, L. Zhang, W. Younas, G. Mao and Q. Liu, *Eur. J. Inorg. Chem.*, 2024, **27**, e202400007.

21 Z. Hao, R. Wang, L. Zhang, X. Liu, H. Li, X. Meng, C. Gu, C. Xia, B. Dong and L. Cao, *Surf. Interfaces*, 2024, **51**, 104667.

22 S. Zhang, P. Du, H. Xiao, Z. Wang, R. Zhang, W. Luo, J. An, Y. Gao and B. Lu, *Angew. Chem. Int. Ed.*, 2023, **136**, e202315763.

23 F. Ye, W. Liu, C. Han, Y. Zhao, P. Liu and H. Wang, *Cryst. Growth Des.*, 2024, **25**, 101-108.

24 S. Li, L. Meng, W. Tian and L. Li, *Adv. Energy Mater.*, 2022, **12**, 2200629.

25 Y. Huang, J. He, W. Xu, T. Liu, R. Chen, L. Meng and L. Li, *Adv. Energy Mater.*, 2024, **14**, 2304376.

26 L. Meng, J. He, X. Zhou, K. Deng, W. Xu, P. Kidkhunthod, R. Long, Y. Tang and L. Li, *Nat. Commun.*, 2021, **12**, 5247.

27 C. Wang, W. Chen, S. Sun, H. Zhang, H. Zhou and S. Li, *Adv. Funct. Mater.*, 2024, **34**, 2313706.

28 Y. Wu, S. Yao, G. Lv, Y. Wang, H. Zhang, P. Liao and Y. Wang, *J. Catal.*, 2021,

401, 262-270.

29 Z. Bao, Y. Jiang, Z. Zhang, J. Lv, W. Shen, J. Dai, J. Wang, J. Cai and Y. Wu, *J. Mater. Chem. A*, 2024, **12**, 15902-15913.

30 I. B. Assaker, M. Gannouni, J. B. Naceur, M. A. Almessiere, A. L. Al-Otaibi, T. Ghrib, S. Shen and R. Chtourou, *Appl. Surf. Sci.*, 2015, **351**, 927-934.

31 B. Fan, Z. Chen, Q. Liu, Z. Zhang and X. Fang, *Appl. Surf. Sci.*, 2016, **370**, 252-259.

32 M. A. Mahadik, P. S. Shinde, M. Cho and J. S. Jang, *Appl. Catal. Environ.*, 2016, **184**, 337-346.

33 M. A. Mahadik, P. S. Shinde, H. H. Lee, M. Cho and J. S. Jang, *Sol. Energy Mater. Sol. Cells*, 2017, **159**, 475-487.

34 Q. Liu, H. Lu, Z. Shi, F. Wu, J. Guo, K. Deng and L. Li, *ACS Appl. Mater. Interfaces*, 2014, **6**, 17200-17207.

35 Z. Bai, X. Yan, Z. Kang, Y. Hu, X. Zhang and Y. Zhang, *Nano Energy*, 2015, **14**, 392-400.

36 Z. Li, K. H. Ng, S. Xu, Y. Zhang, Y. Lei, J. Huang and Y. Lai, *Chemosphere*, 2022, **307**, 135758.

37 L. Meng, D. Rao, W. Tian, F. Cao, X. Yan and L. Li, *Angew. Chem. Int. Ed.*, 2018, **57**, 16882-16887.